

Induced-Charge Electrokinetic Phenomena

Martin Z. Bazant *

* Departments of Chemical Engineering and Mathematics, Massachusetts Institute of Technology, Cambridge, MA 02139 USA

Abstract This chapter provides an introduction to a certain class of nonlinear electrokinetic phenomena, where the applied electric field acts on its own induced-charge in an electrolytic solution near a polarizable surface. Many applications are discussed, such as colloidal particle dynamics (induced-charge electrophoresis) and microfluidic mixing and pumping (induced-charge electro-osmosis), while emphasizing the basic physics of each phenomenon. A Standard Model for these situations is introduced and analyzed in simple cases. Similarities and differences are noted with other electrokinetic phenomena, such as classical linear (fixed-charge) electrokinetics in electrolytes and electrohydrodynamics in leaky dielectrics.

1 Introduction

Electrokinetic phenomena (electrically driven fluid flow and particle motion) in liquid electrolytes have been studied for well over a century in colloid science (Hunter, 2001; Lyklema, 1995; Anderson, 1989), but much recent interest in this classical subject has been triggered by the development of microfluidics (Stone et al., 2004; Squires and Quake, 2005; Laser and Santiago, 2004; Squires, 2009; Schoch et al., 2008). In electrolytes, electrokinetic phenomena are associated with thin electric double layers on charged surfaces, and as a result they have favorable scaling with miniaturization, with increasing surface to volume ratio. Electrokinetic phenomena also offer other unique advantages for “lab-on-a-chip” systems, such as low hydrodynamic dispersion, no moving parts, electrical actuation and sensing, and easy integration with microelectronics. Beyond microfluidics, it is becoming increasingly recognized that electrokinetic phenomena can play an important role in the dynamics of electrified interfaces in other fields such as biology (e.g. vesicle motion, membrane fluctuations, electroporation) and electrochemistry (e.g. porous electrode charging, desalination dynamics, dendritic growth).

Until recently, almost all studies of electrokinetic phenomena have assumed linear response in the applied voltage, based on the hypothesis of fixed surface charge (or fixed “zeta potential” relative to the bulk solution). This assumption is reasonable for most insulating or dielectric surfaces, but not for metallic or ion-conducting surfaces. For applications in microfluidic systems, linear electrokinetic phenomena have a number of possible drawbacks: Direct current (DC) must be passed to sustain electric fields; it is difficult to produce vortices for mixing; and large voltages must be applied along centimeter or greater distances to achieve the necessary field strengths, giving little direct control over local fields and flows within microchannels. Related to these issues, there are also well known drawbacks of linear electrokinetic phenomena in colloid science, e.g. that electrophoresis cannot separate particles with fixed, uniform zeta potential by size or shape in free solution. This is the reason that electrophoretic separation of DNA or other large molecules is usually done in a gel, rather in free solution, to take advantage of entropic effects of trapping rather than differences in electrophoretic mobility.

As shown in Figure 1, much richer dynamics are possible with nonlinear electrokinetic phenomena at polarizable surfaces, which are the focus of this chapter. For recent reviews, see Bazant et al. (2009b), Squires (2009) and Bazant and Squires (2010). The development of this subject in microfluidics began with the discovery by Ramos et al. (1999) of alternating-current electro-osmotic flow (ACEO) over microelectrodes, which Ajdari (2000) showed could be exploited for low-voltage microfluidic pumping using asymmetric arrays of inter-digitated electrodes. These breakthroughs, supported by the early experiments of Green et al. (2000a); González et al. (2000); Green et al. (2002); Brown et al. (2000); Studer et al. (2004) and others, focused attention on nonlinear AC electrokinetics in microfluidics. This work clearly demonstrated that electrokinetic phenomena can derive from non-uniform, transient charge on an electrode surface, controlled more by the applied voltage than by chemical equilibrium.

Bazant and Squires (2004) pointed out that the underlying physical mechanism of an electric field acting on its own induced charge near a polarizable surface is more general and coined the term “induced-charge electro-osmosis” (ICEO) to describe it (Squires and Bazant, 2004). Through a variety of examples, such as those in Fig. 1, they argued that ICEO flows can occur around any polarizable (metal or dielectric) surface in the presence of any (DC or low-frequency AC) electric field – i.e. not exclusively over electrodes whose voltage is directly forced to oscillate at a certain frequency, as in ACEO. The same fundamental physical process, sketched in Figure 2, thus unifies ACEO and travelling-wave electro-osmosis (TWEO)

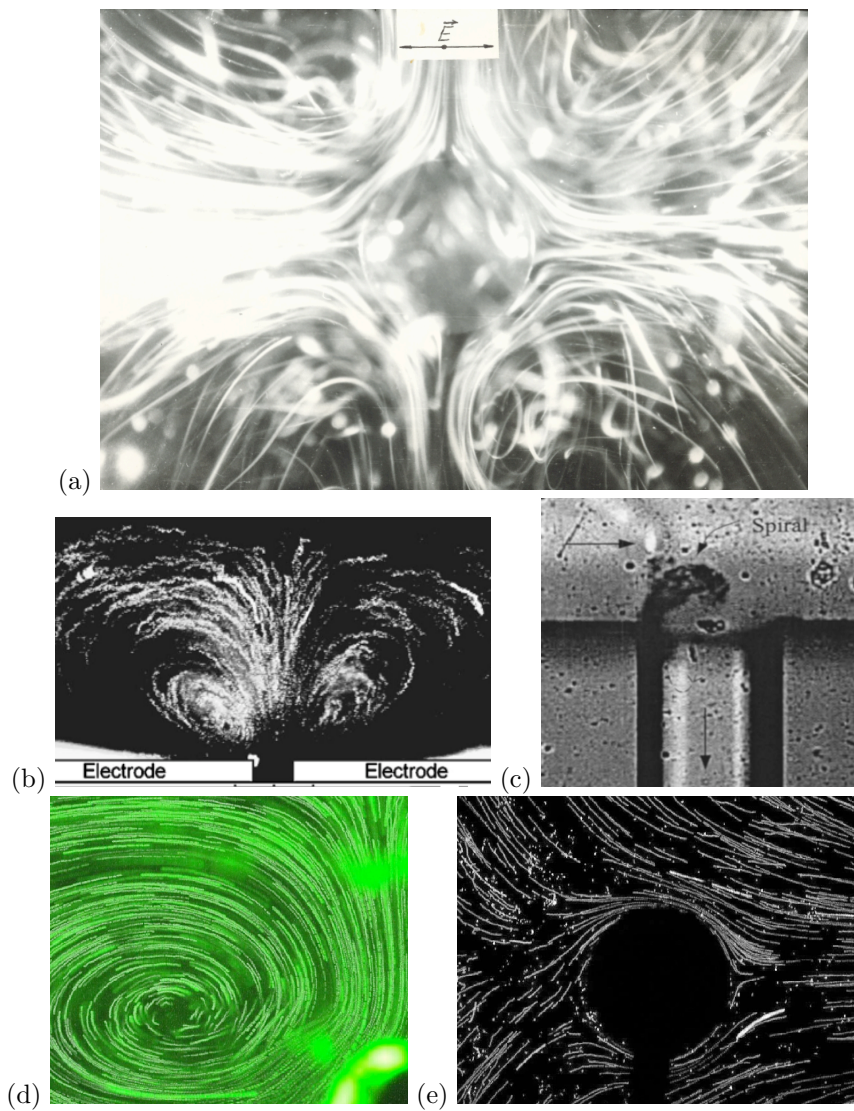


Figure 1. Experimental photographs of induced-charge electro-osmosis, imaged by streaks of tracer particles. (a) Nonlinear flow around a $500 \mu\text{m}$ spherical ionite particle driven by a weak 10 V/cm , 80 Hz background AC electric field, by V. A. Murtsovkin (courtesy of A. S. Dukhin); (b) AC electro-osmosis at a pair of titanium electrodes applying a 2 V 100 Hz AC voltage by Green et al. (2002); (c) DC electrokinetic jet at a dielectric microchannel corner by Thamida and Chang (2002); (d) one roll of quadrupolar ICEO flow around a $100 \mu\text{m}$ cylindrical gold post in a 100 V/cm 300 Hz electric field and (e) fixed potential ICEO flow around a gold post connected to one electrode supplying the background AC field by Levitan (2005). (Reproduced from Bazant (2008b).) 3

(Cahill et al., 2004; Ramos et al., 2005) over micro-electrode arrays (Fig. 2d), with other seemingly unrelated phenomena, such as DC electrokinetic jets at dielectric microchannel corners (Thamida and Chang, 2002) (Fig. 2c), AC electrohydrodynamic interactions and self-assembly of dielectric colloids on electrodes (Trau et al., 1997; Yeh et al., 1997; Nadal et al., 2002; Ristenpart et al., 2003), and hydrodynamic interactions among polarizable particles (Gamayunov et al., 1986; Murtsovkin, 1996) (Fig. 2a).

The latter effect was apparently the earliest example of “ICEO” reported in the literature, from the pioneering work of V. Murtsovkin, A. S. Dukhin and collaborators in the 1980s on polarizable colloids, as reviewed by Murtsovkin (1996), long before analogous ICEO flows were observed in a microfluidic device by Levitan et al. (2005). The quadrupolar ICEO flow around an ideally polarizable sphere in a uniform electric field, and the resulting relative motion of two spheres, were first predicted by Gamayunov et al. (1986). Murtsovkin and collaborators proceeded to observe these flows around mercury drops (Murtsovkin and Mantrov, 1991) and metallic particles (Gamayunov et al., 1992). For larger particles, the flow was in the opposite direction of the theory, which was conjectured to be due to the onset of Faradaic reactions at large induced voltages, consistent with recent experiments on millimeter scale metal objects by Barinova et al. (2008).

The development of microfabrication technology has led to unprecedented control over the geometries of particles and channels, so a major focus of recent research has been on the design of polarizable structures and particles to control, enhance, optimize induced-charge electrokinetic phenomena. The original ACEO micropumps tested in experiments by Brown et al. (2000) and Studer et al. (2004) involved 2D planar arrays of interdigitated electrodes. Bazant and Ben (2006) predicted that faster flows are possible with non-planar stepped electrodes, and such “3D ACEO” designs have since been reduced to practice (Urbanski et al., 2006a,b; Huang et al., 2010). The concept of ICEO mixing by applying electric fields around fixed 3D metal microstructures (Bazant and Squires, 2004; Levitan et al., 2005) is now beginning to be reduced to practice as well (Harnett et al., 2008; Wu and Li, 2008b). ICEO flows around simple 2D metal structures also offer the chance to precisely test the standard model of electrokinetics, as recently shown by Pascall and Squires (2010). Asymmetric geometries of channels and particles also give rise to some surprising phenomena from the classical colloidal standpoint. Bazant and Squires (2004) predicted that an anisotropic particle subjected to a DC or AC field (below the frequency of double-layer charging) will generally translate and/or rotate by “induced-charge electrophoresis” (ICEP), while a fixed anisotropic object will pump the fluid by ICEO (Yariv, 2005; Squires and Bazant, 2006). These nonlinear

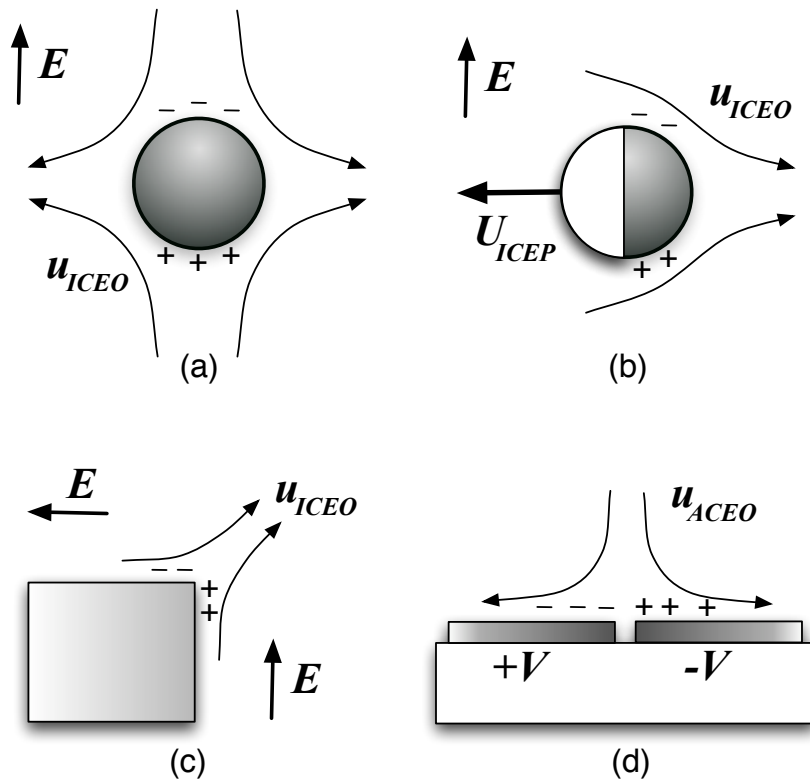


Figure 2. Examples of nonlinear electrokinetic phenomena driven by induced charge (+, -) in the diffuse part of the electrochemical double layer at ideally polarizable, blocking surfaces, subject to an applied electric field E or voltage V . (a) Induced-charge electro-osmosis (ICEO) around a metal post (Bazant and Squires, 2004; Squires and Bazant, 2004; Levitan et al., 2005) or particle (Gamayunov et al., 1986; Murtsovkin, 1996), (b) induced-charge electrophoresis (ICEP) of a metal/insulator Janus particle (Squires and Bazant, 2006; Gangwal et al., 2008), (c) a nonlinear electrokinetic jet of ICEO flow at a sharp corner in a dielectric microchannel (Thamida and Chang, 2002; Yossifon et al., 2006), and (d) AC electro-osmosis (ACEO) over a symmetric pair of microelectrodes (Ramos et al., 1999; Ajdari, 2000; Green et al., 2002). (Reproduced from Bazant et al. (2009b).)

phenomena are very different from classical electrophoresis with surfaces of constant charge and are also beginning to be observed in experiments (Rose and Santiago, 2006; Gangwal et al., 2008).

In this chapter, we survey recent progress in induced-charge electrokinetics and teach the basic physical concepts, theoretical models, and experimental observations. Along the way, we also highlight various open questions for future research.

2 Background

Before discussing nonlinear induced-charge electrokinetic phenomena in electrolytes, we briefly review linear and nonlinear electrokinetic phenomena in weakly conducting liquids, as well as linear (“fixed charge”) electrokinetic phenomena in electrolytes. The latter subject was mainly developed in colloid science over the past century, and there are excellent books available, e.g. by Levich (1962), Dukhin and Derjaguin (1974), Lyklema (1995) and Hunter (2001). Recent application-specific reviews are also available, such as Anderson (1989) and Delgado et al. (2007) on electrophoresis of colloids and Kirby and Hasselbrink (2004) and Tandon and Kirby (2008) on electro-osmosis in microfluidic devices.

2.1 Electrohydrodynamics in dielectric liquids

The term “electrokinetic phenomena” refers to electrically driven fluid flow or particle motion, but it is often used more narrowly, as we do here, to describe fluid or particle motion in electrolytes, consisting of large numbers of dissolved ions in a solvent, typically water. In contrast, the term “electrohydrodynamics” is often used more narrowly to refer to electrokinetic phenomena in low-conductivity dielectric liquids (Melcher and Taylor, 1969; Saville, 1997). A simple example of the latter is the electrophoretic motion of a charged particle in a non-conducting dielectric liquid in a uniform, constant, electric field, as shown in Fig. 3(a). The reader may be familiar with R. Millikan’s famous oil-drop experiment, which first measured the electron charge e a century ago by showing the quantization of the charge $Q = ne$ inferred from the velocities of oil drops suspended in air between capacitor plates, based on the following simple analysis. To calculate the drop velocity \mathbf{U} , the electric force $\mathbf{f}_e = Q\mathbf{E}$ is balanced by the viscous drag force, approximated by Stokes’ formula for a sphere, $\mathbf{f}_d = 6\pi\eta R\mathbf{U}$, where R is the radius and η the fluid viscosity. This force balance yields the scaling of the

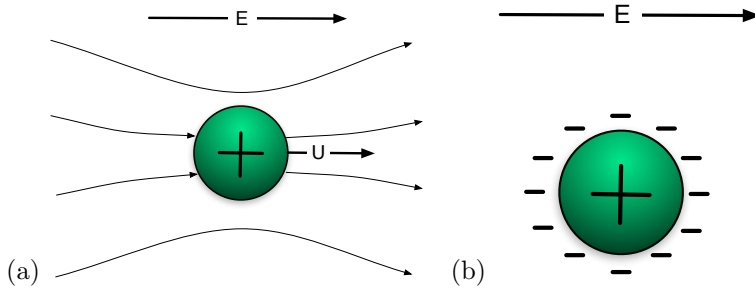


Figure 3. (a) Sketch of the electrophoretic motion of a particle of fixed charge in a non-conducting liquid in a uniform electric field, which drags fluid along with it, analogous to sedimentation under gravity; streamlines are shown in the fixed lab frame of reference. (b) The analogous situation for a charged solid particle in a (conducting) electrolyte, where a thin double layer screens the charge; since the net charge on the interface is zero, no motion results if the fluid velocity is continuous across the interface, as in the Leaky Dielectric Model for liquid drops (Saville, 1997). Instead, particle motion does occur, due to electro-osmotic flow in the double layer, which leads to an effective slip (or velocity discontinuity) over the surface, shown below in Fig. 4.

drop velocity

$$U \propto \frac{Q}{\eta R} \mathbf{E} \quad (\text{electrophoresis in a dielectric liquid}) \quad (1)$$

which is proportional to the electric field and the (fixed) charge, and inversely proportional to the drop size. This is perhaps the simplest example of a “linear” electrohydrodynamic phenomenon, where $U \propto E$.

There can also be nonlinear electrohydrodynamic phenomena in non-conducting liquids. The most familiar example is “dielectrophoresis” (DEP) of polarizable solid particles in non-uniform electric fields (Pohl, 1978; Ramos et al., 1998). The applied field induces a dipole moment on the particle, $\mathbf{p} = \alpha \left(\frac{4\pi}{3} R^3\right) \varepsilon \mathbf{E}$, proportional to its volume and the field, where α is the Maxwell-Wagner factor which depends on electrical properties and, for an AC field, also the frequency. The induced dipole is then pulled by the field gradient toward regions of higher or lower field intensity. The electrostatic force, $\mathbf{f}_e = \mathbf{p} \cdot \nabla \mathbf{E}$, is again balanced by viscous drag \mathbf{f}_d to yield a steady

translational velocity which scales as

$$\mathbf{U} \propto \frac{\varepsilon R^2}{\eta} \nabla E^2 \quad (\text{dielectrophoresis}) \quad (2)$$

The velocity varies with the square of the applied field intensity, and thus survives in an AC field. In uniform DC or AC field, a polarizable particle can also rotate to align its induced dipole with the field axis, in response to the electrical torque, $\mathbf{p} \times \mathbf{E}$, but it cannot translate or rotate continuously.

For weakly conducting liquids, including many oils and non-aqueous solutions, the theory must also account for bulk current and charge accumulation at interfaces. This alters the analysis of electrophoresis and dielectrophoresis and also leads to some new electrohydrodynamic phenomena, directly tied to a non-zero conductivity. Taylor (1966) first described the non-linear deformation of oil drops in electric fields, using what is now called the ‘‘Leaky Dielectric Model’’ (Melcher and Taylor, 1969; Saville, 1997). The applied field drives a small current which induces a charge on the fluid/fluid interface. Although, by symmetry, the drop cannot move, the interfacial induced charge is pulled by the electric field to produce counter-rotating quadrupolar vortices, both inside and outside the drop, while maintaining a continuous fluid velocity at the interface. The flow scales as

$$\mathbf{u} \propto \frac{\varepsilon R E^2}{\eta} \quad (\text{flow around a leaky dielectric drop}) \quad (3)$$

which generally arises in electrohydrodynamics from the balance of electric body force $\rho_e \mathbf{E} \propto$ and the viscous force $\eta \nabla^2 \mathbf{u} \propto \eta u/R^2$, using Poisson’s equation for a linear dielectric response, $\rho_e = \nabla \cdot \varepsilon \mathbf{E} \propto \varepsilon E/R$. Outside the deformed drop, the steady flow resembles the quadrupolar ICEO flow around a solid polarizable particle, in Figs. 1(a) and 2(a). Indeed, below we will encounter the same scaling (3) for ICEO flow around a polarizable particle, but this is clearly a different phenomenon. If Taylor’s liquid drop were replaced by a solid particle, the Leaky Dielectric Model would predict no fluid motion, because the tangential velocity is assumed to be continuous across the interface.

2.2 Electrokinetics in electrolytes

The situation is fundamentally different in an electrolytic solution containing large numbers of dissolved ions. Besides the high conductivity of the bulk electrolyte, ions can easily move to the interface to screen the surface charge, so that the net interfacial charge (for the surface plus its diffuse ionic screening cloud) is zero, as sketched in Figure 3(b). The length scale for this

screening process, where electrostatic attraction is balanced by diffusion, is the Debye screening length,

$$\lambda_D = \sqrt{\frac{\varepsilon k_B T}{\sum_i (z_i e)^2 c_0}} \quad (4)$$

where ε is the permittivity, k_B is Boltzmann's constant, T is the absolute temperature, $z_i e$ are the ionic charges, and c_0 is the bulk neutral salt concentration. In aqueous solutions, the double layers have a tiny extent $\lambda_D = 0.5 - 100$ nm, which is typically much smaller than any geometrical scale L , such as the particle size or microchannel thickness. Such a "thin double layer" with $\lambda_D \ll L$, resembles a capacitor skin on the surface.

In electrolytes with thin double layers, the charge density (per volume) is zero everywhere, including the interface, so how can there be any electrokinetic effects? Indeed, the Leaky Dielectric Model would predict no motion, since there can be no force on an interface of zero net charge. The model also assumes continuity of the velocity field across the interface, which precludes relative motion of the two sides. Electrokinetic effects are readily observed at solid surfaces, however, so clearly an electrolyte is not a standard leaky dielectric.

The flaw in these arguments is that the interface in an electrolyte is a *double layer*, equivalent to a sheet of dipoles, which experiences a nonzero *torque* in a tangential electric field. The electrostatic torque accelerates the fluid on one side relative to the other (fluid or solid) phase, until it is balanced by an opposing viscous torque. In a quasi-steady Stokes flow, this process is instantaneous, and the tangential field produces a steady *electro-osmotic slip*, or velocity discontinuity between the fluid and the surface. This is how Helmholtz (1879) resolved the paradox of electrophoresis in electrolytes with thin double layers, many years after Reuss first observed the electrophoresis of clay particles in water in 1808.

By modeling the double layer as a thin capacitor with a voltage drop ζ from the surface to the bulk solution, Helmholtz derived a simple formula for effective slip across the double layer given by

$$\mathbf{u}_s = -\frac{\varepsilon \zeta}{\eta} \mathbf{E}_{\parallel} \quad (\text{electro-osmotic slip in an electrolyte}) \quad (5)$$

where ε is the permittivity and η the viscosity of the electrolyte, and \mathbf{E}_{\parallel} is the tangential electric field, which is continuous across the interface. This phenomenon of "electro-osmotic flow" forms the basis for electrokinetic phenomena in electrolytes (Hunter, 2001; Lyklema, 1995). In particular, the electrophoresis of a particle with thin double layers in an infinite fluid can

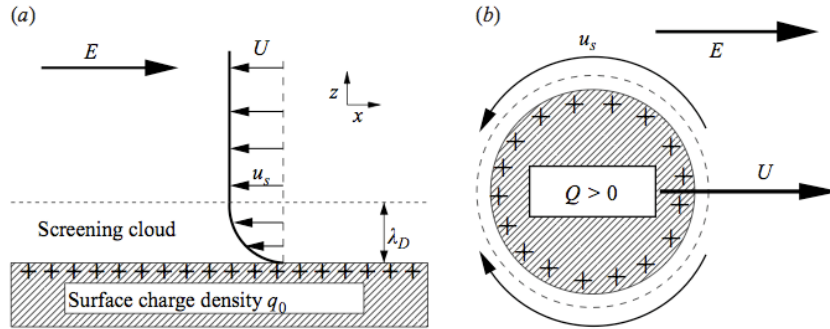


Figure 4. (a) A charged solid surface in an electrolyte attracts a “screening cloud” of excess counter-ions (of the opposite sign) to form a capacitor-like “double layer”. An applied tangential electric field acts on the screening charge to drive electro-osmotic flow parallel to the surface, which builds from no-slip on the walls to an effective nonzero slip velocity outside the double layer. (b) If a particle with thin double layers is freely suspending in an electrolyte, the velocity discontinuity from electro-osmotic flow in an electric field leads to a net swimming motion termed “electrophoresis”. (Reproduced from Squires and Bazant (2004).)

be understood as a phenomenon of “force-free” motion (akin to swimming) in the direction of the applied field due to electro-osmotic slip. Similar phoretic motion can also be driven by gradients in temperature and salt concentration, which also produce tangential gradients in osmotic pressure within the double layer (Anderson, 1989).

Smoluchowski (1905) extended the theory of electro-osmotic flow for diffuse screening charge in the double layer and showed that Eq. (5) holds more generally whenever the fluid permittivity and viscosity are constant across the double layer (using the classical continuum electrokinetic equations). As shown in Fig. 4(a), the tangential fluid velocity builds up exponentially across the diffuse part of the double layer from zero on the surface (assuming no hydrodynamic slip) to u_s outside the double layer. In Smoluchowski’s theory, the zeta potential corresponds to the potential difference between the hypothetical “shear plane” at the inner edge of the diffuse layer and the neutral bulk solution, just outside the double layer, although this need not be the case in more general theories (Bazant et al., 2009b). If the zeta potential is small compared to the thermal voltage, $k_B T/e$ ($= 26$ mV at room

temperature), then the diffuse double layer has a constant capacitance (per area), $C_D \sim \varepsilon/\lambda_D$, as expected for charged parallel plates separated by the screening length (Bazant et al., 2004). In that case, we can recast the electro-osmotic slip formula (5) as

$$\mathbf{u}_s \sim -\frac{\lambda_D q}{\eta} \mathbf{E}_{\parallel}, \text{ if } |e\zeta| \ll k_B T \quad (6)$$

since $C_D = q/\zeta$.

Smoluchowski also considered the motion of colloidal particles with thin double layers ($\lambda_D \ll R$) driven by electro-osmotic flow in applied electric fields, as shown in Fig. 4(b). He showed that a particle with uniform zeta potential (or surface charge) in an infinite fluid translates at a velocity,

$$\mathbf{U} = \frac{\varepsilon\zeta}{\eta} \mathbf{E}_{\infty} \text{ (electrophoresis in an electrolyte)} \quad (7)$$

where \mathbf{E}_{∞} is a uniform background electric field, applied “at infinity”. It can be shown that this result is independent of the shape and size of the particle, assuming thin double layers and uniform ζ , since in the case, the fluid velocity is proportional to the electric field everywhere, $\mathbf{u} \propto \mathbf{E}$, as shown in Fig. 5(a).

For the same reason, a colloid of many such particles will experience zero hydrodynamic interactions (Morrison and Stukel, 1970; Anderson, 1989), as shown in Fig. 5(b). In other words, all the particles will move at the same velocity (7), regardless of the sizes, shapes or concentration. Of course, this can pose a problem for electrophoretic separations of like-charged particles, such as DNA molecules, which explains why DNA electrophoresis is done in a gel in order to exploit entropic (i.e. trapping), rather than purely electrokinetic, effects.

The inability to separate like-charged particles is related to other surprising features of *linear* electrokinetic phenomena involving surfaces of *constant surface charge* (or zeta potential) in electrolytes with thin double layers. A porous medium with these physical properties exhibits the same linear relationship (7) between the mean fluid velocity $\langle \mathbf{u} \rangle = -\mathbf{U}$ and the electric field, regardless of the microstructure. This can be understood as the same effect, if the porous medium is a packed bed of particles held in place, driving flow in the opposite direction of electrophoresis.) The crucial microscopic principle behind these results is that electro-osmotic flow is irrotational, $\nabla \times \mathbf{u} = \mathbf{0}$, in the limit of thin double layers and constant zeta potential, because the fluid velocity is proportional to the electric field, $\mathbf{u} \propto \mathbf{E}$, everywhere in the bulk electrolyte. This is no longer the case if any of these assumptions break down, and it is generally possible to produce

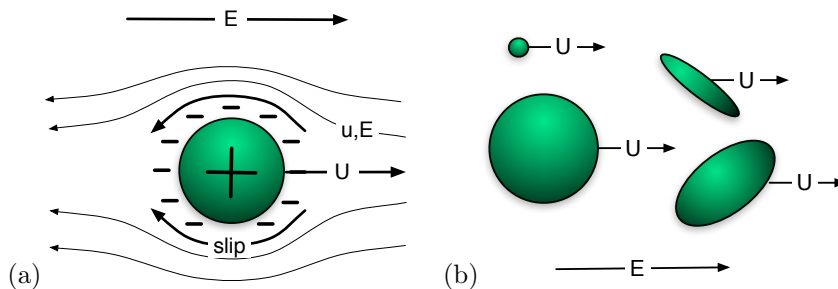


Figure 5. Electrophoresis of particles with thin double layers and constant, uniform surface charge (or zeta potential). (a) The fluid flow in the frame of the moving particle, driven by electro-osmotic slip, is proportional to the electric field, everywhere. (b) As a result, a colloid consisting of many such particles will move at the same velocity as a single particle, regardless of the sizes and shapes of the particles.

vortices by electro-osmosis. In particular, we shall now discuss *nonlinear* ICEO flows involving *polarizable surfaces*, whose charge is not fixed.

3 Principles of Induced-Charge Electrokinetics

3.1 Flows around metal surfaces

The simplest example of ICEO involves a metal sphere (Gamayunov et al., 1986) or cylinder (Bazant and Squires, 2004) in an electrolyte with thin double layers, suddenly subjected to a uniform electric field, sketched in Figure 6. As a first approximation, the sphere is “ideally polarizable”, meaning that its potential is held constant without any Faradaic electron-transfer reactions occurring. Conceptually, there are two steps in the dynamics: (1) electrochemical relaxation of the surface charge in response to the applied field, and (2) electro-osmotic flow around the particle, driven the induced charge.

1. Induced surface charge. When the field is turned on, electrons on the metal surface immediately drift toward one pole to induce a dipole moment, in order to make the surface equipotential (Figure 6a). In a non-conducting dielectric liquid this could be the steady state, but this is an unsteady configuration in an electrolyte. Since the field drives an ionic current, any normal component transports charge in or out of the

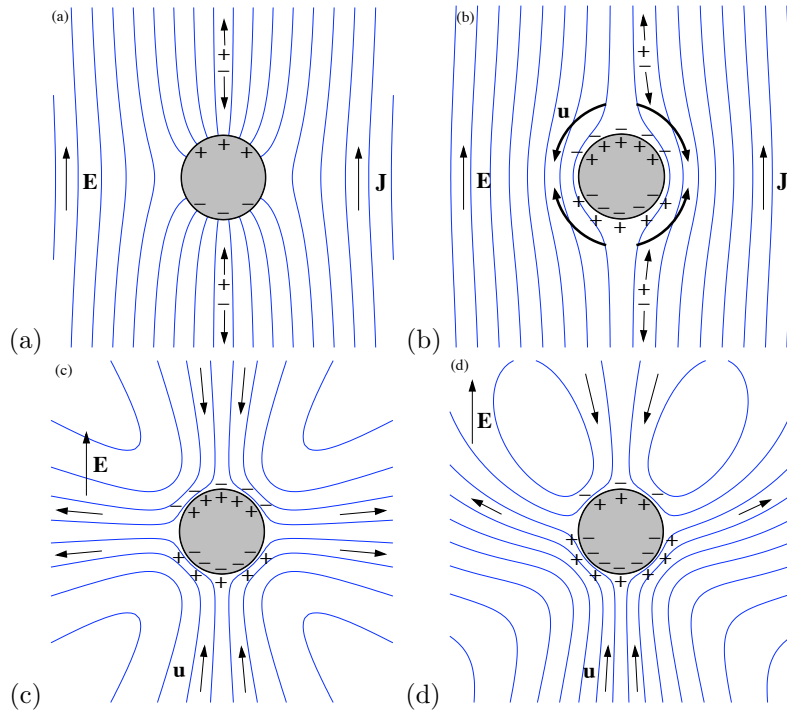


Figure 6. Physical mechanism for induced-charge electro-osmosis around an ideally polarizable metal cylinder in a suddenly applied electric field. (a) When the field is turned on, electronic charges relax to make the surface an equipotential, but the normal current drives double-layer charging. (b) After charging, the field lines are expelled by a nonuniform distribution of induced double-layer charge. (c) The tangential field acts on the induced charge to drive quadrupolar ICEO flow around a neutral cylinder. (d) If the cylinder has a nonzero total charge, then the dipolar flow of linear electrophoresis is superimposed on the quadrupole. (Reproduced from Bazant and Squires (2004)).

diffuse layer. Neglecting surface conduction through the double layer (for thin double layers) and Faradaic reactions passing current through the particle (at low voltage), the normal current locally charges double layer, like a capacitor. This process continues until all the field lines are expelled in steady state (Figure 6b). As first noted by Simonov and Shilov (1977), the basic time scale for this process is the RC time for the equivalent circuit of the bulk resistance (through the solution around the equator) coupled to the diffuse-layer capacitances (on the surface near the poles):

$$\tau_0 = \frac{RC_D}{\sigma} = \frac{\lambda_D R}{D} \quad (8)$$

where σ and D are the bulk conductivity and diffusivity, and R is the particle radius. In more general situations, R is a length scale characterizing the distance between oppositely polarized surfaces, such as an electrode separation (Ramos et al., 1999), as reviewed by Bazant et al. (2004). In microfluidic devices, the typical double-layer charging time τ_0 (\approx ms) is much larger than the Debye relaxation time $\varepsilon/\sigma = \lambda_D^2/D$, for bulk ionic screening (\approx μ s) and much smaller than the diffusion time L^2/D for the relaxation of bulk concentration gradients (\approx s). For nano-channels or nano-particles, however, all of these time scales can be comparable (\approx μ s).

2. Induced electro-osmotic flow. The tangential field acts on the non-uniform induced-charge (or ζ) distribution to produce quadrupolar ICEO flow, sucking fluid at the poles and ejecting it at the equator (Figure 6c). The scaling of the flow can be easily understood as follows. Capacitive charging transmits a non-uniform voltage to the double layer of order ER . If (5) holds, then ICEO flow scales as

$$\mathbf{u}(\mathbf{r}) \propto u_0 = \frac{\varepsilon RE^2}{\eta} \quad (\text{ideally polarizable surface}) \quad (9)$$

which is the same, generic electrohydrodynamic scaling arising in Taylor's flow around a leaky dielectric drop, Eq. (3), as noted above. Unlike linear electro-osmosis, ICEO flow is rotational and depends on the geometry via the size R as well as the shape of the particle (see below). In response to a DC voltage step, the flow approaches the steady state over the RC time scale τ_0 . For AC field of frequency ω , the steady state flow decays above the RC frequency as $[1 + (\omega\tau_0)^2]^{-1}$ (Squires and Bazant, 2004).

From these simple physical arguments, we expect similar flows to be produced around any polarizable object in any electric field, but any *broken symmetry* will generally lead to fluid flow past the object, if it is held fixed, or motion by “induced-charge electrophoresis” (ICEP), if it is freely suspended (Gangwal et al., 2008). If the object has a nonzero total charge Q , as in the case of a charged metal colloidal particle, then the ICEO flow is superimposed on the familiar streaming flow of linear electrophoresis (Figure 6d). Whenever (5) holds, the two effects are additive, since the total charge corresponds to a constant ζ offset, relative to the background potential.

In fixed-potential ICEO, the potential of a polarizable object is controlled so as to induce total charge in phase with a (steady or oscillating) background field (Squires and Bazant, 2004). This effect is essentially an AC generalization of the “flow field effect transistor” (Schasfoort et al., 1999; van der Wouden et al., 2005), similar to the work of van der Wouden et al. (2006). The effective length R above is then set by the distance between the object and the electrodes supplying the background field. As a result, fixed-potential ICEO flow can be much faster than locally produced (e.g. quadrupolar) ICEO flow and has a different frequency response.

Other broken symmetries include irregular shapes (e.g. rods, polyhedra, etc.), non-uniform surface properties (e.g. partial dielectric or metallic coatings), and non-uniform background electric fields (Squires and Bazant, 2006). In each case, net pumping of the fluid by ICEO results if the object is held fixed, which requires a certain force and torque. Conversely, if the object is a colloidal particle, then broken symmetries cause it to translate and rotate by ICEP, as described below.

3.2 Flows around dielectric surfaces

The canonical example above assumes an ideally polarizable surface, where the double layer charges capacitively to sustain the entire voltage applied to the object, but the phenomenon of ICEO is more general and occurs at any polarizable surface, to varying degrees (Squires and Bazant, 2004). For example, if the metal object described above has a thin dielectric coating of width h_S and permittivity ε_S , then both the time scale (8) and the flow scale (9) are multiplied by a factor $\Lambda = (1 + \delta)^{-1}$, where

$$\delta = \frac{C_D}{C_S} = \frac{\varepsilon}{\varepsilon_S} \frac{h_S}{\lambda_D} \quad (10)$$

is the ratio of the dielectric-layer capacitance to the diffuse-layer capacitance, which are placed in series in an equivalent circuit for the double layer. This shows that dielectric coatings thicker than the Debye length can substantially reduce ICEO flows at metal surfaces. In the limit of a purely

dielectric object of characteristic length scale, $R \gg \lambda_D$, ICEO flow scales as

$$\mathbf{u} = \frac{\varepsilon_S \lambda_D E^2}{\eta} \quad (\text{dielectric surface}) \quad (11)$$

which is smaller than for an ideally polarizable object by a factor $\delta \gg 1$.

Although often small, ICEO flows at dielectric surfaces need not be negligible in microfluidic devices, since there can be large local electric fields at sharp geometrical features. As shown in Figure 1(c), an electric field passing around a sharp corner in a dielectric microchannel can drive a strong nonlinear electrokinetic jet of ICEO flow due to the corner field singularity (Thamida and Chang, 2002; Yossifon et al., 2006). In very simple terms, illustrated in Fig. 2(c), this phenomenon can be understood as half of the quadrupolar flow around a polarizable particle, where the jet corresponds to the outward flow at the equator in Figure 6(c).

As noted above, dielectric objects also experience electrostatic forces, leading to DEP motion of freely suspended particles. The uniform component of a background electric field induces a dipole on the object, which then feels a torque to align it with the field. A field gradient applies a force to the induced dipole. Higher-order multipoles in the background field can likewise cause forces and torques by acting on higher-order induced multipole moments on the object. In the case of colloidal dielectric particles, these forces and torques (balanced by hydrodynamic drag) produce translational velocity $u \sim \varepsilon R^2 \nabla E^2 / \eta$ and rotational velocity $\Omega \sim \varepsilon E^2 / \eta$ of DEP, respectively. The theory of DEP has mostly been developed for dielectric liquids, but in electrolytes ICEO flows also occur, with the very same scalings with field and particle size (Squires and Bazant, 2006). The net electrokinetic motion of polarizable particles in non-uniform fields results from a competition between DEP and ICEP, originally termed “dipolophoresis”, which was first analyzed for colloidal spheres by Shilov and Simonova (1981).

4 Standard Model for thin double layers

The mathematical description of ICEO flows began with the pioneering work of Murtsovkin (1996) on metallic colloids and Ramos et al. (1999) and Ajdari (2000) on AC pumping of liquids by micro-electrode arrays. Bazant and Squires (2004) unified these theories in a simple “Standard Model”, derivable from the full Poisson-Nernst-Planck (PNP) equations of ion transport and Navier Stokes equations of viscous fluid flow in the asymptotic limit of thin double layers (DL), compared to geometrical length scales. The model is based on the assumption of “linear” or “weakly nonlinear” charging dynamics (Bazant et al., 2004), which further requires that the applied volt-

age is small enough not to significantly perturb the bulk salt concentration, whether by double-layer salt adsorption or Faradaic charge-transfer reaction currents. By neglecting Faradaic reactions, we focus on “blocking” or “ideally polarizable” metal surfaces. In the same limit, surface conduction through the diffuse part of the double layers can also be neglected (Chu and Bazant, 2007; Khair and Squires, 2008), unless there is a large pre-existing fixed charge, upon which a small perturbation is induced, as described by Murtsovkin (1996).

With these assumptions, the problem is greatly simplified, and the electrokinetic problem decouples into one of electrochemical relaxation, similar to Leaky Dielectric Model (Saville, 1997), and another of viscous flow, driven by electro-osmotic slip. Although this model can be rigorously justified only for very small voltages, $\Psi_D \ll kT/e$, in a dilute solution (González et al., 2000; Squires and Bazant, 2004), it manages to describe many features of ICEO flows at much larger voltages. Extensions of the model for large voltages are reviewed by Bazant et al. (2009b) and discussed at the end of this chapter.

4.1 Electrochemical relaxation

The first step in the Standard Model is to solve Laplace’s equation for the electrostatic potential across the bulk resistance,

$$\nabla \cdot \mathbf{J} = \nabla \cdot (\sigma \mathbf{E}) = 0 \quad \Rightarrow \quad \nabla^2 \phi = 0 \quad (12)$$

assuming Ohm’s Law with a constant conductivity σ . For a blocking polarizable surface, which cannot pass a normal current, a capacitance-like boundary condition closes the equivalent RC circuit:

$$\frac{dq}{dt} = \hat{\mathbf{n}} \cdot \mathbf{J} \quad \Rightarrow \quad C \frac{d\Psi}{dt} = \sigma \hat{\mathbf{n}} \cdot \nabla \phi, \quad (13)$$

where $-q$ is the total surface charge (equilibrium + induced), q is the screening charge, $\Psi = \phi_0 - \phi$ is the local double-layer voltage drop from the metal surface at ϕ_0 to the bulk solution just outside the double layer at ϕ , and C is the total differential capacitance of the double layer, also assumed to be constant. A simple and important special case of (13) is the low-frequency or DC limit, $\hat{\mathbf{n}} \cdot \nabla \phi = 0$, where the surface behaves like an insulator since the double layer is fully charged and cannot sustain any normal current (since we neglect surface conduction and Faradaic reactions).

The potential of the surface ϕ_0 is either controlled externally, in the case of an electrode, or determined self-consistently by the condition of fixed total charge Q integrated over the surface, in the case of a freely suspended

colloidal particle:

$$Q = \oint_S d\mathbf{r} \int_0^{\Psi(\mathbf{r})} C(\psi) d\psi \quad (14)$$

where we allow for nonlinear response of the double layer, via a voltage-dependent capacitance, $C(\Psi)$. Examples of such nonlinear extensions of the Standard Model are discussed below and reviewed by Bazant et al. (2009b). In the limit of linear response with a constant capacitance, valid for small voltages $|e\Psi| \ll k_B T$, the total charge is proportional to the surface-averaged double-layer voltage

$$Q \sim C \oint_S d\mathbf{r} \Psi(\mathbf{r}) \quad (15)$$

which implies

$$\phi_0 \sim \bar{\phi}_0 + \langle \phi \rangle \quad (16)$$

where $\bar{\phi}_0 = Q/CA$ is the surface potential assuming a constant capacitance over the area $A = \oint_S d\mathbf{r}$ and $\langle \phi \rangle = \oint_S d\mathbf{r} \phi(\mathbf{r})/A$ is the surface-averaged potential in the solution, just outside the double layer. In symmetric problems involving uncharged colloids ($Q = 0$), it is common to set $\phi_0 = \langle \phi \rangle$, but this is only valid for linear response to a small induced double-layer voltage. More generally, Equation (14) is a nonlinear integral constraint, which self-consistently determines the potential of a metal particle, ϕ_0 .

4.2 Fluid flow

After solving for the electrostatic potential ϕ , the second step in the Standard Model is to solve for the fluid velocity \mathbf{u} satisfying the unsteady Stokes equations for creeping flow,

$$\rho_m \frac{\partial \mathbf{u}}{\partial t} = -\nabla p + \eta \nabla^2 \mathbf{u}, \quad \nabla \cdot \mathbf{u} = 0, \quad (17)$$

where ρ_m is the mass density. The unsteady term is only important to describe transient flows at high frequencies, where momentum diffusion becomes comparable with mass diffusion. For steady AC response or low frequency transients, this term is generally neglected.

Since it is assumed that the bulk electrolyte remains quasi-neutral with constant conductivity, there is no body force on the fluid in (17). Instead, coupling to the electrochemical problem only arises through the Helmholtz-Smoluchowski boundary condition (5) of effective fluid slip outside the double layer,

$$\mathbf{u}_s = \mathbf{u} - \mathbf{U} - \mathbf{r} \times \boldsymbol{\Omega} = -\frac{\varepsilon \Psi_D}{\eta} \mathbf{E}_{\parallel} \quad (18)$$

where \mathbf{E}_{\parallel} is the tangential field and Ψ_D is the voltage from the “shear plane” (where the velocity vanishes) to the bulk solution (Lyklema, 1995). The slip velocity represents a tangential velocity discontinuity between \mathbf{u} , the fluid velocity just outside the double layer, and $\mathbf{U} + \mathbf{r} \times \boldsymbol{\Omega}$, the velocity of the solid surface, where \mathbf{U} and $\boldsymbol{\Omega}$ are the local translational and rotational velocities, which are either prescribed or determined by mechanical constraints, as described below. The assumption of uniform bulk salt concentration allows us to neglect tangential osmotic pressure gradients, which modify the slip formula with a term for diffusio-osmotic flow (Rubinstein and Zaltzman, 2001; Zaltzman and Rubinstein, 2007).

To close the model, following Green et al. (2002), it is common to assume that only a constant fraction $\Lambda \leq 1$ of the double-layer voltage falls across the diffuse screening cloud: $\Psi_D = \Lambda\Psi$. The simplest model of ICEO flow assumes $\Lambda = 1$, i.e. all of the double-layer voltage drop contributes to the induced zeta potential. In that case, the theory has no adjustable parameters, but it tends to over-estimate ICEO flows, sometimes by orders of magnitude compared to experimental data. As shown in Fig. 7, some experimental data can be fitted fairly well by allowing Λ to be an adjustable parameter. See Table 1 of Bazant et al. (2009b) for a summary of Λ values extracted from a wide range of experiments on different induced-charge electrokinetic phenomena and a discussion of the limitations of this approach.

The great simplification of the Standard Model is that the full nonlinear Poisson-Nernst-Planck/Navier-Stokes equations are replaced by two *linear* boundary-value problems, which are amenable to analytical solutions in many cases and more convenient for numerical solutions. First, the potential ϕ is obtained by solving the linear problem (12)-(13), and this allows the slip velocity profile (18) to be calculated. The fluid velocity \mathbf{u} and pressure p are then obtained by solving another linear problem (17)-(18). This procedure avoids solving a nonlinear problem because the slip boundary condition (18) is linear in \mathbf{u} and only nonlinear in ϕ , which can be solved separately, without knowing \mathbf{u} in advance.

4.3 Particle motion

The total mechanical force \mathbf{F} and torque \mathbf{T} acting on any body are related to the electric field and fluid velocity profiles via integrals over an

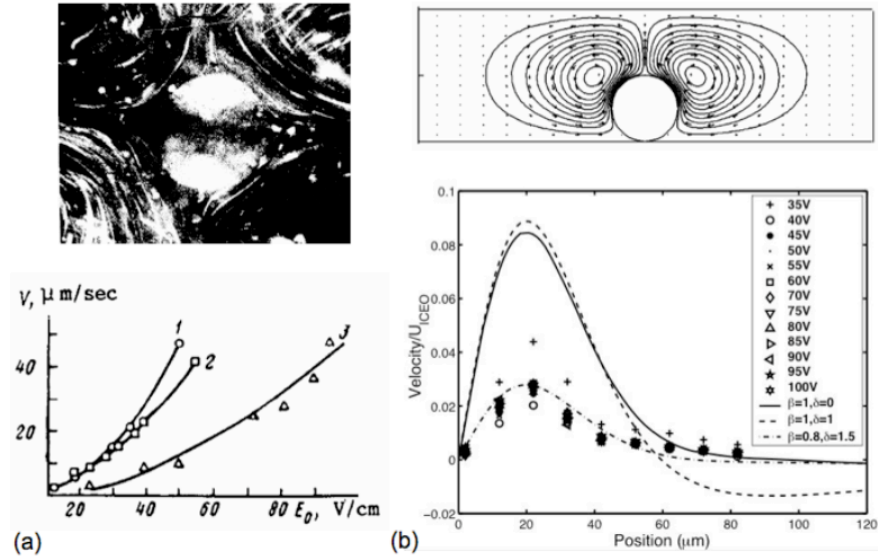


Figure 7. Early tests of the Standard Model for ICEO flows around metal objects in AC electric fields. (a) ICEO flow around a tin colloidal particle (photograph above); experimental data by Gamayunov et al. (1992) for the fluid velocity sampled at different points around the particle (top) versus the field strength, which demonstrated the quadratic scaling of Eq. (9), but not any details of the flow profile. (b) The velocity profile around a $100 \mu\text{m}$ platinum cylinder in a microchannel, simulated by the Standard Model (above) and compared with measurements by micro-particle-image velocimetry (below) by Levitan et al. (2005); a horizontal slice of the velocity profile $5 \mu\text{m}$ above the wire at different voltages shows good data collapse with the scaling (9); a reasonable fit is obtained with $\Lambda = 1/(1 + 1.5) = 2/5$ using (26), and a better fit (without accounting for ion adsorption) can be obtained using a constant-phase-angle impedance model. (Reproduced from Bazant (2008b).)

enclosing surface S ,

$$\mathbf{F} = \int_S d\mathbf{r} \hat{\mathbf{n}} \cdot \boldsymbol{\sigma} \quad (19)$$

$$\mathbf{T} = \int_S d\mathbf{r} \mathbf{r} \times (\hat{\mathbf{n}} \cdot \boldsymbol{\sigma}) \quad (20)$$

of the stress tensor,

$$\sigma_{ij} = -p \delta_{ij} + \eta \left(\frac{\partial u_j}{\partial x_i} + \frac{\partial u_i}{\partial x_j} \right) + \varepsilon \left(E_i E_j - \frac{1}{2} E^2 \delta_{ij} \right) \quad (21)$$

where δ_{ij} is the unit tensor. The first term in (21) is the isotropic pressure tensor; the second is the viscous stress tensor for a Newtonian fluid; and the third is the Maxwell stress tensor for a linear dielectric medium of constant permittivity. In the case of steady state flow (or time-averaged periodic flow, described below), the Stokes equation (17) expresses local mechanical equilibrium, $\nabla \cdot \mathbf{T} = 0$, so the bounding surface S can be deformed arbitrarily to any convenient shape to calculate the force and torque integrals. For example, for a bounded collection of colloidal particles in an infinite fluid, it is usually best to deform S to infinity.

For fixed geometries in microfluidic devices, the translational and rotational velocities \mathbf{U} and $\boldsymbol{\Omega}$ of solid boundaries are set to zero. The integrals (20) and (20) then give the force \mathbf{F} and torque \mathbf{T} exerted by the fluid on the solid, which are equal and opposite to the force and torque needed to hold the solid in place, respectively.

For a freely suspended colloidal particle, the situation is more subtle. In a quasi-steady Stokes flow, the translational and rotational velocities, \mathbf{U} and $\boldsymbol{\Omega}$, are determined implicitly by the constraints that there be no net force, $\mathbf{F} = 0$, and no net torque, $\mathbf{T} = 0$, exerted on the particle by the fluid, since there is negligible translational and angular acceleration, respectively. This assumes that viscous dissipation is strong enough to neglect the inertial term, $\mathbf{u} \cdot \nabla \mathbf{u}$, and fast enough (compared to other relaxation times or the AC period) to neglect the unsteady term, $\partial \mathbf{u} / \partial t$, in the Navier-Stokes equations.

In practice, the translation and rotational dynamics of a particle can be calculated as follows (Kilic and Bazant, 2007). In the Standard Model, the linearity of the bulk Stokes flow (outside the double layers) allows us to express the fluid velocity as a superposition of two flows:

1. the electro-osmotic flow (\mathbf{u}_s, p_s) resulting from the slip profile (18) around a fixed particle with $\mathbf{U} = \boldsymbol{\Omega} = \mathbf{0}$, which exerts a force \mathbf{F}_s and torque \mathbf{T}_s on the particle;

2. the purely viscous flow (\mathbf{u}_v, p_v) with $\mathbf{E} = \mathbf{0}$ resulting from the particle's motion \mathbf{U} and $\mathbf{\Omega}$, which exerts \mathbf{F}_v and \mathbf{T}_v on the particle.

These flows are subject to the constraints, $\mathbf{F} = \mathbf{F}_s + \mathbf{F}_v = \mathbf{0}$ and $\mathbf{T} = \mathbf{T}_s + \mathbf{T}_v = \mathbf{0}$, which implicitly determine \mathbf{U} and $\mathbf{\Omega}$. In nontrivial geometries involving asymmetric particles or nearby channel walls, there is generally a coupling between translation and rotation due to viscous flow, which can be expressed as

$$\begin{pmatrix} \mathbf{F}_v \\ \mathbf{T}_v \end{pmatrix} = \mathbf{M}_v^{-1} \begin{pmatrix} \mathbf{U} \\ \mathbf{\Omega} \end{pmatrix} \quad (22)$$

where \mathbf{F}_v and \mathbf{T}_v are the force and torque exerted by the fluid on the particle, due only to its motion, and \mathbf{M}_v is a mobility tensor, taking into account viscous dissipation in the instantaneous geometry. The inverse tensor \mathbf{M}_v^{-1} is a generalization of the drag coefficient, e.g. $6\pi\eta R\mathbf{I}$ for a sphere in an infinite fluid, and can be calculated by solving Stokes equations with no slip on a moving and rotating particle and then performing the integrals (20) and (20) for the force and torque.

Armed with the particle's mobility tensor, \mathbf{M} , the particle motion can then be determined from

$$\begin{pmatrix} \mathbf{U} \\ \mathbf{\Omega} \end{pmatrix} = -\mathbf{M}_v \begin{pmatrix} \mathbf{F}_s \\ \mathbf{T}_s \end{pmatrix} \quad (23)$$

where \mathbf{F}_s and \mathbf{T}_s are the force and torque on the particle (electrostatic + viscous) in response to the slip profile around a fixed particle in the same position. In a numerical simulation, these equations can be iterated to self consistency in an implicit scheme, or \mathbf{M}_v , \mathbf{F}_s , and \mathbf{T}_s can be calculated once using \mathbf{E} , \mathbf{U} and $\mathbf{\Omega}$ from the previous time step, or by interpolation to the new time step, in an explicit scheme.

4.4 Symmetric geometries

For certain symmetric geometries, the reciprocal theorem for Stokes flow can be used to avoid having to actually solve the Stokes equations, if one only wants to calculate the motion of the solid body. For a spherical particle with an arbitrary slip distribution $\mathbf{u}_s(\mathbf{r})$ on its surface, Stone and Samuel (1996) showed that the translational velocity is equal and opposite to surface-averaged the slip velocity:

$$\mathbf{U} = -\frac{\oint_S d\mathbf{r} \mathbf{u}_s(\mathbf{r})}{\oint_S d\mathbf{r}} \quad (24)$$

while the rotational velocity is given by

$$\boldsymbol{\Omega} = -\frac{\oint_S d\mathbf{r} \hat{\mathbf{r}} \times \mathbf{u}_s(\mathbf{r})}{2 \int_V d\mathbf{r}} \quad (25)$$

where V is the volume of the particle. Squires and Bazant (2006) pointed out that the same relations also hold for cylindrical geometries, in spite of various subtleties of two-dimensional Stokes flows. (Note that we have written (25) in a different form, which clarifies this connection.) These results make it much easier to solve for the motion of inhomogeneous particles with symmetric shapes (and variable surface properties), rather than for homogeneous particles with asymmetric shapes. As in many mathematical problems, complicated boundary conditions are more tractable than complicated geometries.

An analogous result to (24) also holds for fluid pumping in a parallel-plate microchannel with arbitrary slip distributions on both surfaces. The total flow rate through the channel is the same as that of a linear shear flow driven by the surface-averaged slip on the two walls, or, equivalently, a plug flow $\mathbf{u}_{plug} = -\mathbf{U}$ driven by the overall average slip (over both walls) from (24). This property was noted by González et al. (2000) in the context of a Fourier analysis of AC electro-osmotic pumping with periodic slip, but it holds more generally for any slip profile, as shown by Squires (2008). Most theoretical studies of slip-driven microfluidic pumping have used this property to calculate the time-averaged flow rate, without having to solve for the time-averaged velocity field, but it can only be applied to flat plate geometries. For three-dimensional electrodes, as discussed below, one must solve the full Stokes flow to obtain the flow rate.

5 Double-layer models

A microscopic model of the double layer is required to predict how the capacitance C and voltage Ψ_D (or Λ) in the Standard Model depend on experimental conditions, such as the bulk salt concentration and the interfacial chemistry. Most studies of ICEO flow have adopted the classical two-part model of the double layer (Bockris and Reddy, 1970), which adds a molecular-scale “compact part” described by boundary conditions between the surface and the outer “diffuse part” described by continuum equations for mobile ions. It is typically assumed that the electrokinetic (zeta) potential Ψ_D is the same as the diffuse-layer potential drop from the edge of the compact layer to the bulk solution. This sharp partitioning of the double layer into two distinct regions is convenient for mathematical modeling, but not precisely defined. In principle, many features of the molecular compact

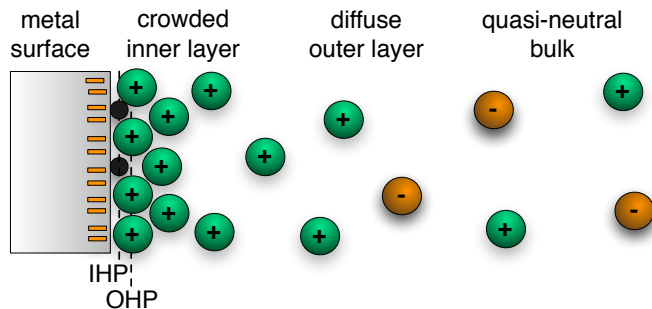


Figure 8. Sketch of the double layer near a blocking electrode at high voltage. Solvated counterions (green) are crowded in the inner region and smoothly transition across the outer diffuse region to a dilute solution with solvated anions (orange). An ion can break free from its solvation shell and adsorb on the surface (black), thereby moving from the outer Helmholtz plane (OHP) to the inner Helmholtz plane (IHP). (Reproduced from Bazant et al. (2009b).)

layer can be reproduced by more realistic continuum models of the diffuse layer accounting for ion-specific effects, such as steric volume constraints, dielectric saturation, and the viscoelectric effect Bazant et al. (2009a,b).

The concept of the compact layer was introduced by Stern (1924) to account for the finite solvated ion size in the simplest possible way, by positing a distance of closest approach of solvated ions to the surface h_S , at the “outer Helmholtz plane” (Bockris and Reddy, 1970) shown in Fig. 8. After separating a layer of thickness h_S from the continuum region, it is also convenient to assign it a reduced permittivity $\epsilon_S < \epsilon$ to describe dielectric saturation (aligning of solvent dipoles) in the large normal field in the innermost portion of the double layer. Stern’s model effectively adds capacitance $C_S = \epsilon_C/h_S$ in series with the diffuse-layer capacitance C_D . The concept of a “surface capacitance” in series with the bulk solution is quite general and not limited to a Stern monolayer of aligned solvent molecules. It could also describe a thin dielectric coating on the surface, such as an oxide layer, contaminant film, self-assembled polymer monolayer, etc.

The resulting simple model,

$$\frac{C}{C_D} = \Lambda = \frac{1}{1 + \delta} \quad (\text{Stern layer or dielectric coating}) \quad (26)$$

has only one fitting parameter $\delta = C_D/C_S$ in (10) to describe the the

physical properties of double layer (Ajdari, 2000; Green et al., 2002; Bazant et al., 2004; Levitan et al., 2005; Olesen et al., 2006). Note that the time scale (8) for double-layer charging is generally reduced by the same factor as the capacitance, $\tau/\tau_0 = C/C_D$. This model has been widely applied to ICEO flows, but it is unable to fit detailed experimental measurements in microfluidic devices without some additional modification of the boundary conditions, as shown in Fig. 7. It also fails to predict the strong decay of ICEO flow with increasing concentration and various flow reversals that can occur at large voltage and/or large frequency (Bazant et al., 2009b). It is becoming clear that the simplest version of the Standard Model (26) is incomplete, but simple extensions are being developed that improve the agreement with experiments, at least in the regime of small diffuse-layer voltages where the Standard Model has theoretical justification.

Another important role of the compact layer is to mediate the adsorption/desorption of ions, which react with ionizable sites on the surface and thus regulate the surface charge. The storage of charge by specific adsorption of ions introduces an effective “chemical” capacitance of the double layer *in parallel* with its “physical” capacitance due to purely electrostatic effects (van Hal et al., 1996). In the case of deprotonization reactions in water, the surface effectively buffers the pH of the solution, so this parallel capacitance is sometimes called the “buffer capacitance” (van der Wouden et al., 2006). We will more generally refer to it as the “adsorption capacitance” C_A .

Pascall and Squires (2010) recently showed that including the adsorption capacitance is essential to fit experimental data for ICEO flows over metal electrodes with silica coatings, as shown in Figures 9 and 10. In their version of the Standard Model, C_A is in parallel with C_D , and the pair is in series with C_S :

$$\frac{C}{C_D} = \frac{1 + \beta/\delta}{1 + \delta + \beta}, \quad \Lambda = \frac{1}{1 + \delta + \beta}, \quad (\text{ion adsorption on dielectric}) \quad (27)$$

where $\beta = C_A/C_S$ is a second dimensionless parameter, taken to be constant in a given experiment. This model is reasonable for their experiments where C_A represents the deprotonization of silanol groups on the silica coating, $\text{SiOH} \leftrightarrow \text{SiO}^- + \text{H}^+$ and C_S represents a dielectric layer, much thicker than the molecular scale, inserted between the surface and the electrolyte.

For bare metal surfaces, however, the situation is different, as sketched in 8. In that case, C_A describes desolvated ions adsorbed on the surface at the “inner Helmholtz plane”, while C_S represents the dielectric response of the Stern solvent monolayer up to the first layer of solvated ions at the “outer Helmholtz plane” (OHP) (Bockris and Reddy, 1970). In that case, the

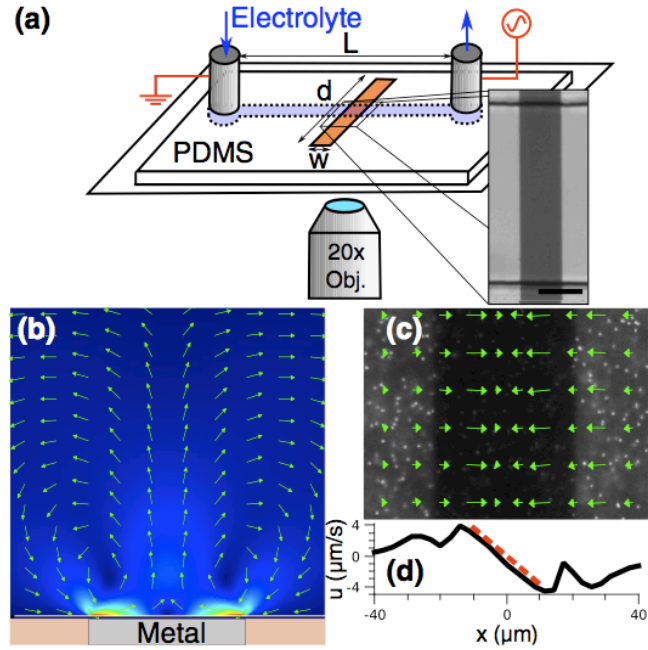


Figure 9. Experimental setup of Pascall and Squires (2010) to measure ICEO flows at high throughput with different surfaces. A planar gold strip ($50\mu\text{m}$) sits perpendicular to a PDMS microchannel (a), along which an AC field is applied, driving two counter-rotating ICEO rolls in aqueous KCl solutions, as simulated by the Standard Model (b). Micro-PIV velocity measurements just above the strip (c) recover the predicted ICEO slip velocity varying linearly with distance from the strip center (d). (Reproduced from Pascall and Squires (2010))

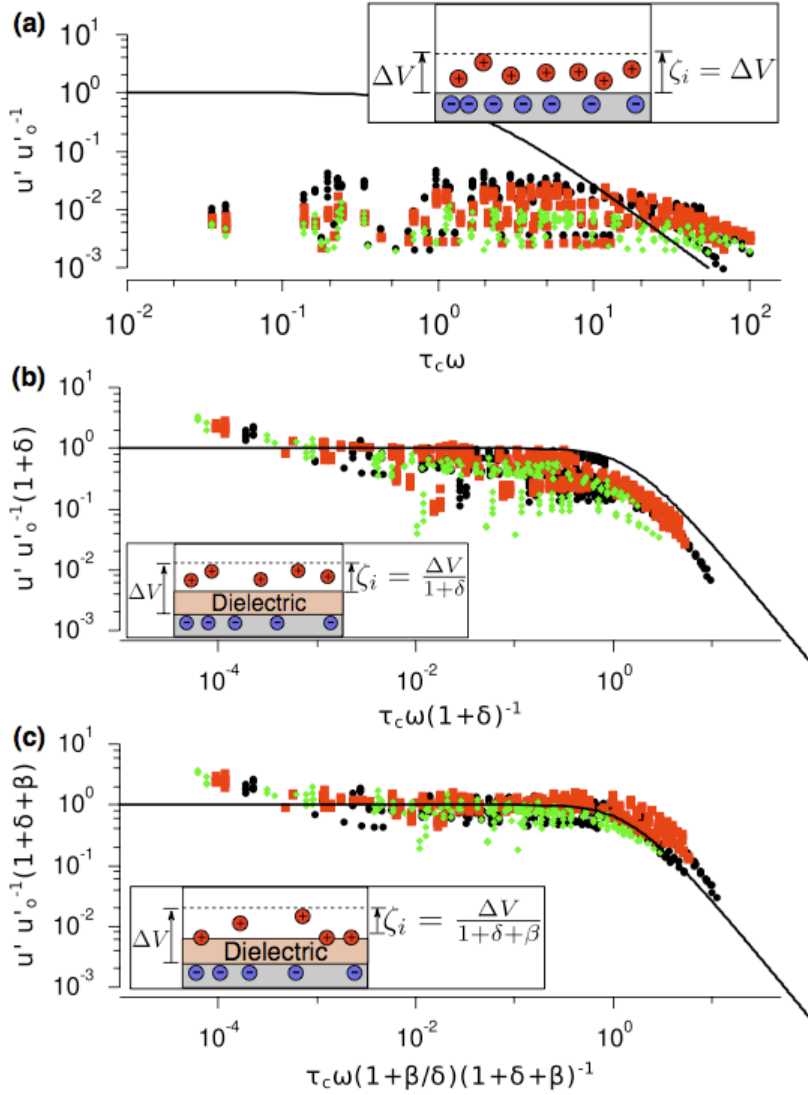


Figure 10. Experimental validation of the Standard Model of ICEO flow using the setup of Figure 9. Measurements over gold strips “controllably contaminated” with SiO₂ films for 987 conditions of varying thickness (33–100 nm) and frequency ω show poor agreement with a theory that ignores the SiO₂ (a), improved agreement when the known surface capacitance of the film is included via $\delta = C_D/C_S$ (b), and remarkable collapse when the adsorption capacitance of SiOH deprotonization is included via $\beta = C_A/C_S$ (c). (Reproduced from Pascall and Squires (2010))

Stern layer does not separate the adsorbed ions from the surface, as shown in Fig. 8, so it is more reasonable to place the adsorption capacitance C_A in parallel with the total physical capacitance of C_D and C_S in series, leading to

$$\frac{C}{C_D} = \frac{\beta}{\delta} + \frac{1}{1+\delta}, \quad \Lambda = \frac{1}{1+\delta} \quad (\text{ion adsorption on bare metal}) \quad (28)$$

in place of (27). It appears that this simple model with constant δ and β has not yet been applied to ICEO flows, but more sophisticated models of potential-dependent ion adsorption have recently been developed by Suh and Kang (2008) and successfully fit to the ACEO pumping data of Green et al. (2002) by Suh and Kang (2009).

It is important to note that the capacitance of the double layer generally depends on the interfacial voltage, due to the *nonlinear* electrochemical response of ions in the diffuse layer, as well as adsorption and reaction kinetics in the compact layer. See Bazant et al. (2009b) for a recent review, in the present context of induced-charge electrokinetics. For example, long ago, Grahame (1947) showed that the total differential capacitance of mercury drop electrodes in aqueous solutions can be well described using the Gouy-Chapman model for the nonlinear differential capacitance of the diffuse layer in a dilute symmetric binary electrolyte,

$$C_D(\Psi_D) = \frac{\varepsilon}{\lambda_D} \cosh\left(\frac{ze\Psi_D}{2k_B T}\right) \quad (29)$$

placed in series with a (fitted) nonlinear compact-layer capacitance, which depends only on the state of charge, but not the bulk salt concentration (Bockris and Reddy, 1970). The Gouy-Chapman-Stern model assumes a constant compact layer capacitance in series with $C_D(\Psi_D)$ from (29), so that $C(\Psi) = (C_S^{-1} + C_D(\Psi_D)^{-1})^{-1}$ in the RC boundary condition (13). Such nonlinear effects have also been included in some Standard Model calculations as the first correction to the linear response theory, but the most common approximation is a constant capacitance C for the double layer, although this can only be rigorously justified for small voltages, $|ze\Psi_D| \ll k_B T$.

6 AC forcing

6.1 The complex potential

It is common to study ICEO flows under alternating current (AC) conditions at driving frequency ω . In that case, the Standard Model with constant double-layer capacitance can be placed in a simple time-dependent

form, following González et al. (2000) and Levitan et al. (2005). We neglect transient vorticity diffusion within each period and focus only on deriving the time-averaged flow profile $\langle \mathbf{u} \rangle$ in a periodic steady state, which satisfies the steady Stokes equations,

$$\nabla p = \nabla^2 \langle \mathbf{u} \rangle, \quad \nabla \cdot \langle \mathbf{u} \rangle = 0 \quad (30)$$

due to the linearity of the unsteady equations.

We begin by switching to dimensionless variables. We scale length to the geometrical scale R and time to the RC charging time $\tau = (C/C_D)\tau_0$ in Eq. (8). The dimensionless frequency is $\omega\tau$. For an applied field amplitude E , we scale the potential to ER , and velocity to Λu_0 in Eq. (9). These scalings contain all the information about the chemical and physical properties of the system using the definitions above, leaving only one parameter in the equations, the dimensionless frequency, $\omega\tau$. In the remainder of this section, we abuse notation and use the same variables to represent their dimensionless counterparts, to keep the presentation simple.

For constant double-layer capacitance, the electrochemical relaxation problem is linear, so the response to any periodic forcing is simply a linear superposition of the response to individual Fourier modes at frequency ω . To solve for a particular Fourier mode, we introduce the dimensionless *complex potential amplitude*, Φ , defined by

$$\phi(\mathbf{r}, t) = \text{Re} \{ \Phi(\mathbf{r}) e^{i\omega t} \} \quad (31)$$

The real part of the complex amplitude, $\text{Re}\Phi$, represents the response which is in phase with the forcing, while the imaginary part, $\text{Im}\Phi$ is the out-of-phase response. Both parts are harmonic functions,

$$\nabla^2 \Phi = 0 \quad (32)$$

subject to the boundary conditions $\hat{\mathbf{n}} \cdot \nabla \Phi = 0$ on an insulating surface and

$$i\omega(\Phi - \Phi_0) = \hat{\mathbf{n}} \cdot \nabla \Phi \quad (33)$$

on an ideally polarizable surface at complex potential Φ_0 .

More generally, we should write

$$\Phi - \Phi_0 = Z(\omega) \hat{\mathbf{n}} \cdot \nabla \Phi \quad (34)$$

where $Z(\omega)$ is the (dimensionless) impedance of the double layer (Barsoukov and Macdonald, 2005). Our simple capacitor model corresponds to $Z = (i\omega)^{-1}$. Green et al. (2002) and Levitan et al. (2005) have also

considered “constant-phase-angle impedance”, $Z = (i\omega)^p$, with a fitted exponent $p < 1$. This model was found to improve the fit of their experimental data for bare metal surfaces, as shown in Fig. 7(b) (where $p = \beta$), and also helped to fit independent cell impedance measurements. It is difficult to interpret the data unambiguously, however, since the microscopic justification of constant-phase-angle impedance is controversial, and other effects, such as ion adsorption (see below), were neglected.

Once the time-independent linear boundary-value problem (32)-(33) is solved for $\Phi(\mathbf{r})$, we can solve the linear Stokes equations (30) for the time-averaged velocity profile, $\langle \mathbf{u}_s \rangle$, subject to no-slip on the insulating surfaces and a time-averaged ICEO slip boundary condition,

$$\langle \mathbf{u}_s \rangle = -\frac{1}{4} \nabla_{\parallel} |\Phi - \Phi_0|^2 \quad (35)$$

on the polarizable surfaces, which is linear in the unknown velocity, but nonlinear in the known potential. Levitan et al. (2005) derived Eq. (35) with $\Phi_0 = 0$ for a symmetric geometry with a cylindrical metal wire at potential. For the general case of an electrode or metal structure with $\Phi_0 \neq 0$, the (dimensionless) oscillating slip velocity is

$$\mathbf{u}_s = -\Psi_D \mathbf{E}_{\perp} = \text{Re} \{ (\Phi_0 - \Phi) e^{i\omega t} \} \text{Re} \{ \nabla_{\perp} \Phi e^{i\omega t} \} \quad (36)$$

Using $\text{Re} z = (z + \bar{z})/2$ and averaging over a time period, we find

$$\langle \mathbf{u}_s \rangle = \frac{1}{4} [(\Phi_0 - \Phi) \nabla_{\perp} \bar{\Phi} + (\bar{\Phi}_0 - \bar{\Phi}) \nabla_{\perp} \Phi] \quad (37)$$

The desired result (35) follows for a metal surface whose potential is constant in space (but not time), so that $\nabla_{\perp} \Phi_0 = 0$.

6.2 Analytical example: Metal sphere in an AC field

To demonstrate the ease of applying the our general mathematical framework, we derive the formula of Murtsovkin (1996) for the frequency-dependent flow around an ideally polarizable colloidal sphere in a uniform AC field (neglecting surface conduction). Many other examples appear in the literature cited above and in recent reviews (Bazant et al., 2009b; Squires, 2009; Bazant and Squires, 2010), but this canonical example serves to illustrate the basic steps in any analysis of ICEO flow with the Standard Model.

We work with dimensionless variables in spherical coordinates (r, θ, φ) with length scaled to the sphere radius R and voltage scaled to E_{∞}/R , where E_{∞} is the uniform field strength far from the sphere. By symmetry the solution depends only on (r, θ) , and we can set the sphere potential to

zero $\Phi_0 = 0$ relative to the background applied potential. The solution to Laplace's equation (32) satisfying the far field boundary condition,

$$\mathbf{E} = -\nabla\Phi \sim \cos\omega t \hat{z}, \quad r \rightarrow \infty \quad (38)$$

has the form

$$\Phi(r, \theta) = -r \cos\theta \left(1 + \frac{p}{r^3}\right) \quad (39)$$

where the first term represents the uniform background field and the second the induced dipole on the particle and its screening cloud. The (dimensionless) complex induced dipole moment,

$$p = \frac{1 - i\omega}{2 + i\omega}, \quad (40)$$

is obtained by imposing the RC boundary condition (33). Consistent with the simple physical arguments in Fig. 6, the metal particle behaves like a bare conductor at high frequency, $\lim_{\omega \rightarrow \infty} p = -1$, and like an insulator at low frequency, $\lim_{\omega \rightarrow 0} p = 1/2$, due to complete screening by the induced double layer. The former is due to electron charge separation in the particle, required to make the particle an equipotential surface with a normal electric field, while the latter is the result of ionic charge relaxation in the double layers, which fully expels the normal electric field.

The complex dipole moment (40) captures the time-dependent polarization of the particle and its screening cloud in response to the AC forcing (Dukhin and Shilov, 1980). The real part is the in-phase polarization,

$$\text{Re } p = \frac{2 - \omega^2}{4 + \omega^2} \quad (41)$$

which transitions from $1/2$ at low frequency to -1 at high frequency, and passes through zero at $\omega_c = \sqrt{2}$. At this critical frequency, only the uniform background electric field remains, as if the particle were “invisible” in phase with the AC forcing. The out-of-phase polarization

$$\text{Im } p = -\frac{3\omega}{4 + \omega^2} \quad (42)$$

reaches a maximum at ω_c , due to capacitive charging of the double layers on opposite sides of the particle, carried by ionic currents passing through the bulk electrolyte resistance to complete an equivalent RC circuit (Simonov and Shilov, 1977). These time-dependent polarization phenomena are also seen in more complicated geometries, as illustrated in Fig. 11 below.

The time-averaged electro-osmotic slip profile on the sphere is easily calculated from (35) as

$$\langle u_\theta(1, \theta) \rangle = \left(\frac{9}{4} \right) \frac{\sin 2\theta}{4 + \omega^2} = U_s(\omega) \sin 2\theta \quad (43)$$

which drives a quadrupolar Stokes flow with angular and radial components

$$\langle u_\theta(r, \theta) \rangle = \frac{U_s(\omega) \sin 2\theta}{r^4} \quad (44)$$

$$\langle u_r(r, \theta) \rangle = \frac{U_s(\omega)(1 + 3 \cos 2\theta)}{2} \left(\frac{1}{r^4} - \frac{1}{r^2} \right) \quad (45)$$

respectively.

As in Fig. 6, the long-ranged part of the ICEO flow, decaying as r^{-2} , is a radial flow that sucks fluid in toward the poles of the sphere and ejects fluid away from the equator. The flow has a longer range than classical electro-osmotic flow, decaying as r^{-3} , although still a shorter range than forced electrophoresis (Fig. 3(a)), decaying as r^{-1} . Gamayunov et al. (1986) first calculated this flow for $\omega = 0$ and noted how the long-range part dominates the interaction between two polarizable colloidal particles, causing them to move together (or apart) if aligned parallel (or perpendicular) to the field axis. The same anisotropic hydrodynamic interactions due to ICEO flow are also evident in the Brownian-dynamics simulations of Saintillan et al. (2006a) and the experiments of Rose and Santiago (2006) for rod-like metal particles in a uniform electric field.

6.3 Numerical example: Metal cylinder in a microchannel

Microfluidic devices involved bounded channel geometries, which make analytical progress difficult in most cases. (Exceptions include simple geometries in two dimensions, amenable to conformal mapping analysis following Yossifon et al. (2006).) Nevertheless, the formalism above, based on the Standard Model with AC forcing, is still useful to reduce the full, time-dependent, nonlinear equations to a relatively simple time-independent form, involving only the linear Laplace and Stokes equations. Aside from dealing with the non-standard boundary conditions, it then becomes straightforward to solve the problem using well known algorithms or common software packages.

An example of the numerical solution of the model using the Finite Element Method is shown in Figure 11, using the package, FEMLAB, a precursor of COMSOL Multiphysics. The simulations describe the ICEO flow around an ideally polarizable metal cylinder lying on the floor of a flat

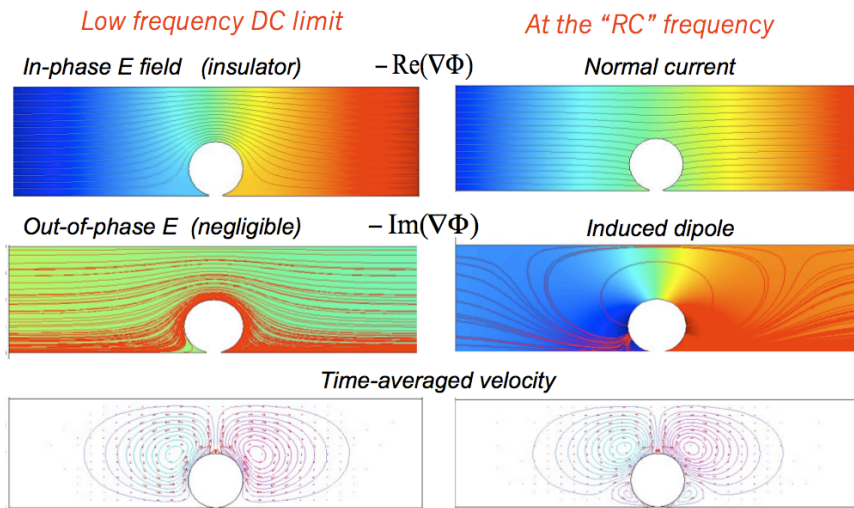


Figure 11. Finite-element numerical solution of the Standard Model for AC forcing from Section 6.1 for the experimental geometry of Levitan et al. (2005), consisting of a 100-micron diameter metal cylinder in a straight microchannel with an longitudinal applied field. Top row: electric field lines in phase with the AC forcing (gradient of the real part of the complex potential). Middle row: field lines 90° out of phase with the forcing (gradient of the imaginary part). Bottom row: streamlines of the time-averaged ICEO flow. Left column: Zero frequency (DC, steady state). Right column: Unit dimensionless frequency $\omega\tau = 1$, where the AC period equals the “RC time” of the equivalent circuit. A slice of the computed flow profile in this figure is compared to experimental data in Figure 7(b) above. (Simulations by Y. Ben from Levitan et al. (2005).)

microchannel, whose height is twice the cylinder’s diameter. An AC electric field is applied along the microchannel, perpendicular to the orientation of the cylinder. This is the geometry of the experiments of Levitan et al. (2005), which were the first to demonstrate ICEO flow around an electrically floating object (whose voltage is not controlled as an electrode) in a microfluidic device. This study was also able to make the first quantitative comparison of the theoretical flow profile, computed numerically, with experimental data, taken by particle-image velocimetry, as shown in Fig. 7.

The simulations in Fig. 11 nicely illustrate the physical principles in Fig. 6 and show similar frequency-dependent behavior as the analytical solution of the previous section:

- At low frequency ($\omega\tau \ll 1$), the AC period is long enough to allow complete charging of the double layer in phase with the forcing. As a result, the in-phase electric field ($\text{Re}\nabla\Phi$) resembles that of an insulator in a DC field, going around the cylinder, while the out-of-phase field ($\text{Im}\nabla\Phi$) is negligible. The time-averaged ICEO flow is directed from the poles of the cylinder toward the equator, but due to the nearby no-slip wall, only half of the quadrupolar flow for an isolated cylinder (Fig. 6) is visible. The bounded geometry also causes the flow to recirculate in two counter-rotating vortices.
- At the transition frequency ($\omega\tau = 1$), the AC period is in resonance with the relaxation of the double layer. As a result, the in-phase electric field is almost unaffected by the presence of the cylinder, and the out-of-phase field lines show the induced dipole with two lobes emanating from the cylinder. The time-averaged flow now shows the appearance of secondary, small vortices completing a quadrupolar structure, due to incomplete charging of the double layers, which has not had enough time to proceed between the poles and the wall.
- At high frequency ($\omega\tau \gg 1$, not shown), there is not enough time for double-layer charging, and the in-phase field resembles that of a perfect conductor in a DC field, where the cylinder remains an equipotential surface, even outside the double layers. Since there is little charge relaxation, the out-of-phase field and ICEO flow are negligible.

These three frequency regimes are generally present for all ICEO flows around a polarizable surface, driven by a weak AC field in the electrolyte. More complicated microfluidic geometries can lead to a distribution of charging time scales, and thus additional frequency regimes, where ICEO flows develop in different locations for different ranges of frequencies.

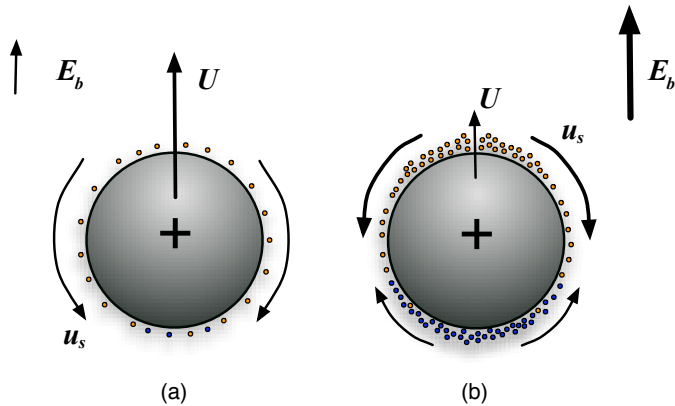


Figure 12. Field-dependent electrophoretic velocity U of an ideally polarizable, charged sphere of radius R with thin double layers in a background field E . (a) In small fields, the mobility $\mu_{ep} = U/E$ is a constant, set by the uniformly distributed double-layer charge. (b) In large fields, $E \gg kT/eR$, the dipolar induced charge overwhelms the pre-existing uniform charge and alters the mobility, $\mu_{ep}(E)$, if cations and anions do not condense at the same density and must redistribute to conserve total charge. (Reproduced from Bazant et al. (2009b).)

7 Electrophoresis of ideally polarizable particles

7.1 Field-dependent mobility and aperiodic electrophoresis

A well-known prediction of the classical theory of electrophoresis is that the mobility (7) only depends on the total charge (or average zeta potential), in the limits of thin double layers, small charge, and weak fields (Hunter, 2001; Anderson, 1989). This remarkable result holds for any size or shape, even if the particle is polarizable and acquires a non-uniform charge (or zeta) profile in response to the applied field. It is not widely appreciated, however, that this follows from the assumption of linear response of the double layer with a constant capacitance, which reduces (14) to (16)

In the 1970s, S. S. Dukhin's group was perhaps the first to recognize that the electrophoretic mobility of polarizable particles must generally depend on the electric field (Dukhin and Dukhin, 2005). In a series of Russian papers, which have yet to gain widespread attention, they predicted perturbations of the electrophoretic mobility as, $\Delta\mu_{ep} \propto E^2$, and thus nonlinear

electrokinetic motion, $\Delta U \propto E^3$, which they have come to call the “Stotz-Wien effect”.

One general mechanism for nonlinear electrophoresis in steady DC fields, first predicted by A. S. Dukhin (1993), is a voltage-dependent double-layer capacitance. In the limit of weak applied electric fields, $E \ll kT/eR$, he showed that an ideally polarizable sphere with equilibrium zeta potential ζ_0 and radius R has a field-dependent DC electrophoretic mobility,

$$\mu_{ep}(E) = \frac{U(E)}{E} \sim \frac{\varepsilon}{\eta} \left(\zeta_0 - \frac{3}{8} \frac{C'_D(\zeta_0)}{C_D(\zeta_0)} (ER)^2 + \dots \right) \quad (46)$$

where ζ_0 is the surface averaged diffuse layer voltage, $\langle \Psi_D \rangle$. This result follows directly from the Standard Model formalism developed above, by applying perturbation methods to Eq. (14). The same equations could be used to analyze the frequency dependence and shape dependence of this effect, but apparently this has not yet been done.

Dukhin’s correction (46) has mainly been applied in the context of the Gouy-Chapman model, Eq. (29), which predicts decreased mobility, $\Delta\mu_{ep} < 0$ since $dC_D/d\psi > 0$ for $\zeta_0 > 0$. It has also recently been derived as the small field limit of a general formula for thin double layers with the Gouy-Chapman model by Yariv (2008). The same formula was also derived by Bazant et al. (2009b) as the dilute limit of a still more general theory that also accounted for the significant influence of finite ion sizes at high voltage (see below).

The basic physics of this nonlinear effect is illustrated in Fig. 12. If the double-layer voltage varies enough to cause spatial variations in its differential capacitance, then counterions aggregate with varying density (per area) around the surface of the particle upon polarization by the applied field, and this nonlinearity breaks symmetry in polarity with respect to the mean voltage. For example, if the positively charged part of the diffuse layer (relative to the mean charge) is less dense (e.g. due to larger or less charged cations than anions), it will cover more of the surface than the negatively charged part; cations are then more likely to dominate in regions of large tangential field near the equator and thus make an enhanced contribution to the electrophoretic mobility of the particle, regardless of its true surface charge.

Dukhin and Dukhin (2005) have proposed a general means to exploit of field-dependent mobility of colloidal particles for separations by “aperiodic electrophoresis”. The basic idea is to use an “unbalanced AC field”, whose time-average is zero, $\langle E \rangle = 0$, but whose higher moments are nonzero. (The same concept, without reference to a particular mechanism for field-dependent mobility, apparently first appeared in a 1992 U.S. patent of Chi-

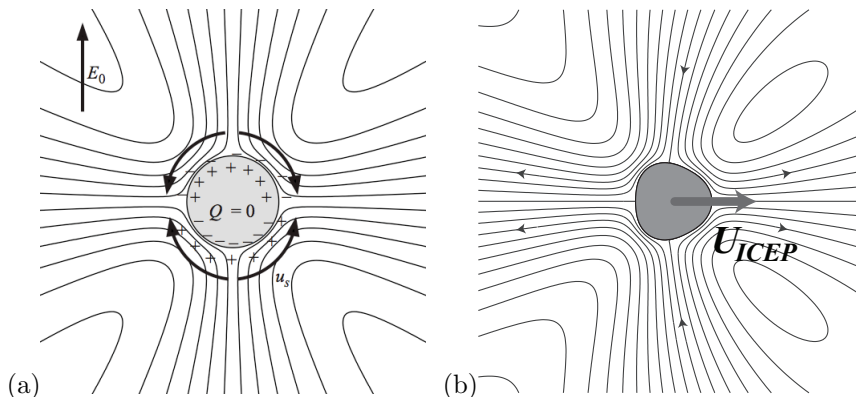


Figure 13. (a) Induced-charge electro-osmotic (ICEO) flow around a symmetric, uncharged, ideally polarizable particle (from Bazant and Squires (2004)); (b) An example of ICEO flow and the resulting induced-charge electrophoretic (ICEP) velocity for an asymmetric shape (from Ref. 4). Due to broken left-right symmetry, the unbalanced ICEO flows cause the particle to move perpendicular to the electric field, which would not be possible due to electrostatic forcing alone. (Reproduced from Squires and Bazant (2006).

menti, Ser. No. 5,106,468.) If $\langle E^3 \rangle \neq 0$, then Dukhin's first correction to the mobility (46) survives time averaging and leads to separation of particles with different polarizabilities. An example of such an unbalanced field is

$$E = E_1 \sin(\omega t) + E_2 \sin(2\omega t + \varphi) \quad (47)$$

where φ is a phase shift, which can be conveniently varied to control the time-averaged motion of a particle. Analyzing and exploiting this effect in practical separations would be an interesting direction for research.

7.2 Induced-charge electrophoresis

Mobility perturbations for spherical particles only hint at the rich phenomena that can arise in the electrokinetic motion of polarizable particles. Murtsovkin (1996) and co-workers were the first (and to date, perhaps the only ones) to experimentally observe the nonlinear electrokinetic motion of homogeneous particles in a uniform AC field in directions oblique to the field axis. They studied irregular quartz particles moving in water near the wall of a cuvette in surprising directions apparently set only by the particle

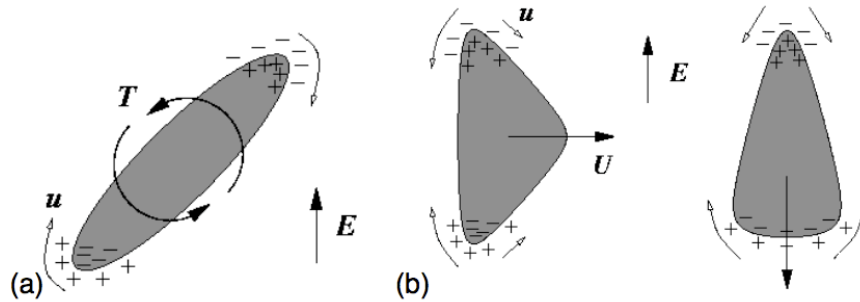


Figure 14. (a) Mechanism for ICEP torque on a rod-like, polarizable particle in a uniform electric field, which enhances dielectrophoretic (DEP) torque. (b) Possible ICEP velocities for asymmetric shapes, once their long axes have aligned with the field.

shape. If a particle rotated enough by Brownian motion when the field was off, it could be seen to reverse direction when the field was turned back on. The velocity scaled with the square of the field amplitude and increased with the particle size. No theory was proposed for this phenomenon, in part since it was only observed near the wall and not in the bulk solution.

Bazant and Squires (2004) recently predicted that polarizable particles in the bulk can undergo essentially arbitrary translation and/or rotation by “induced-charge electrophoresis” (ICEP) in a uniform electric field, as long as they possess appropriate broken symmetries (Squires and Bazant, 2006), such as non-spherical shapes and/or non-uniform surface properties, e.g. due to coatings of varying polarizability. The former cases begin to explain Murtsovkin’s early observations and beg for new experiments to test a variety of specific theoretical predictions, discussed below. The latter cases, first observed by Gangwal et al. (2008), are described in the next section on heterogeneous particles.

For homogeneous particles, the canonical example is that of an uncharged, ideally polarizable particle of irregular shape in a weak, uniform DC field. In that case, the basic velocity scale U_0 is given by Eq. (9), where R is a characteristic radius scale. Using the Standard Model (with constant double-layer capacitance), Yariv (2005) general expressions for the

translational and rotational velocities, respectively,

$$E_i = U_0 \sum_{jk} C_{ijk} E_j E_k \quad (48)$$

$$\Omega_i = \frac{U_0}{a} \sum_{jk} D_{ijk} E_j E_k \quad (49)$$

where C is a dimensionless tensor and D a pseudo-tensor, each expressible as surface integrals involving the bulk potential, just outside the double layer. Squires and Bazant (2006) treated a number of specific examples by solving the Standard Model equations analytically using boundary perturbation methods for nearly symmetric objects, and they developed simple principles to predict the motion of a particular shape.

The basic mechanism of ICEP for irregular particles is shown in Figure 13. As shown in (a) and described above, the ICEO flow around a symmetric particle is quadrupolar, drawing fluid in along the field axis and ejecting it radially. If the particle has broken left/right symmetry as shown in (b), then the radial flow is stronger on one side than the other, leading to ICEP motion perpendicular to the field. Such unusual motion cannot result from electrostatics alone, since there is no charge distribution which can experience an electrostatic force transverse to a uniform electric field. Similarly, breaking only fore/aft symmetry produces ICEP motion along the field axis, and combinations of these asymmetries can cause motion in an arbitrary direction.

ICEP can also contribute to the rotation of polarizable particles with elongated shapes, as illustrated in Figure 14(a). It is well known that DEP causes such particles to align with the axis of a uniform field, due to electrostatic torque on the induced dipole. At low AC frequency (or in the DC limit), if the field persists in one direction long enough for ICEO flow to occur, then ICEP causes a rotational velocity with a basic scale U_0/R that is independent of the particle size but sensitive to its shape,

$$\Omega \propto \frac{\varepsilon E^2}{\eta} \quad (50)$$

This scale happens to be the same as that of the DEP rotational velocity, so ICEP rotation is easily overlooked and mistakenly interpreted as DEP. It is possible, however, to clearly distinguish the two effects, as recently demonstrated by experiments of Rose and Santiago (2006) and simulations of Saintillan et al. (2006a) involving rod-like, metal particles in uniform AC fields. See Figure 15(a).

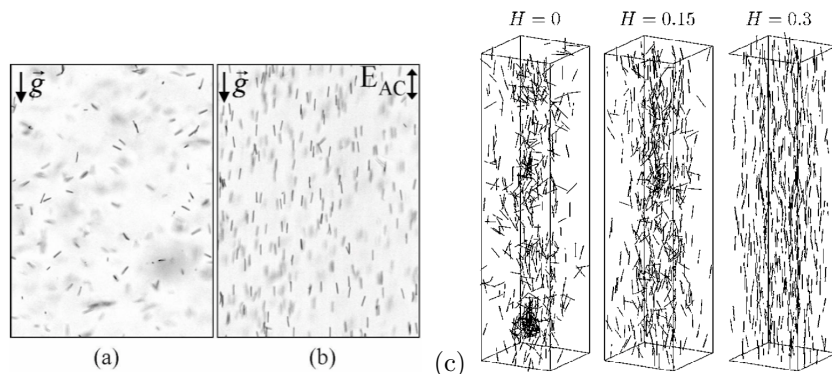


Figure 15. Experiments on cylindrical silver particles ($.318\mu\text{m}$ diameter, $6\mu\text{m}$ length) sedimenting in de-ionized water by gravity alone (a) and in a 100 Hz, 100 V/cm AC field aligned with gravity (b). (Reproduced from Rose and Santiago (2006).) The experimental distribution of angles in different fields is well described by the Standard Model, taking into account both ICEP rotation and DEP electrostatic torque. (c) Brownian-dynamics simulations show the suspension of sedimenting rods can be stabilized by ICEO flows upon increasing the field strength (H). (Reproduced from Saintillan et al. (2006b).)

More complicated asymmetric particles can undergo essentially arbitrary ICEP motion, even in a uniform field. Even in the context of the simple model above, these effects have not yet been fully analyzed, but some general principles have been identified by Squires and Bazant (2006). A striking example is shown in Figure 14(b), which illustrates how arrow-like particles of slightly different shapes can move in perpendicular directions in a uniform field, depending on their broken symmetries: On the left, a short, fat arrow rotates to align its long axis with the field and then moves perpendicular to the field, toward its pointed end; on the right, a long, thin arrow also rotates to align its long axis, but then moves parallel to the field, toward its blunt end. Such predictions are quite recent, however, and remain to be tested experimentally.

A telltale sign of ICEP is the presence of non-uniform ICEO flow around the particle, which leads to complex hydrodynamic interactions with other particles and walls. For example, the basic quadrupolar flow in Figure 13(a) causes two symmetric particles to move toward each other along the field axis and then push apart in the normal direction, as first shown by

Gamayunov et al. (1986). A finite cloud of such particles would thus become squashed into a disk-like spreading pancake perpendicular to the field axis (Squires and Bazant, 2004). Hydrodynamic interactions between particles due to ICEO flows are also able to stabilize a suspension of sedimenting rods, above a critical field strength, as shown in Fig. 15(c) from the work of Saintillan et al. (2006b).

The basic ICEO flow field can also cause particles to be repelled from insulating walls (perpendicular to the field), as noted by Zhao and Bau (2007a), or attracted toward electrodes (normal to the field), but these are only guiding principles. Broken symmetries in particle shape or wall geometry, however, can cause different motion due to combined effects of DEP and ICEP, even opposite to these principles, and the interactions of multiple particles can also be influenced strongly by walls. Such effects have not yet been fully explored in experiments or simulations.

7.3 Dipolophoresis

In the 1970s, Shilov and Estrella-Lopis first recognized that electrohydrodynamics (what we now call ICEO) can contribute to the motion of particles in low-frequency, non-uniform electric fields (Simonova et al., 2001), in addition to the classical effect of DEP, although the effect has not been studied much in theory or experiment. Shilov and Simonova (1981) analyzed the problem of an ideally polarizable sphere in a uniform field gradient and made the remarkable prediction that the particle does not move. Due to equal and opposite motions by DEP and ICEP, the sphere levitates in the field while driving a steady ICEO flow, but this is a unique case.

Squires and Bazant (2006) showed that broken symmetries in the field gradient and/or the particle shape generally cause a particle to move, due to subtle imbalances between ICEP and DEP. Both effects have the same basic scaling (2). Moreover, as shown in Figure 16, the DEP force and ICEP velocity tend to act in opposite directions, at least for the case of an ideally polarizable particle with thin double layers in a non-uniform electric field (of arbitrary complexity). Similar to the case of rotational motion discussed above, ICEP can be easily overlooked and the observed translational motion attributed solely to DEP, if it is along the field gradient. Experiments clearly separating ICEP and DEP effects are still lacking, and an opportunity exists to exploit these combined effects for manipulating polarizable colloids, once the effects are better understood.

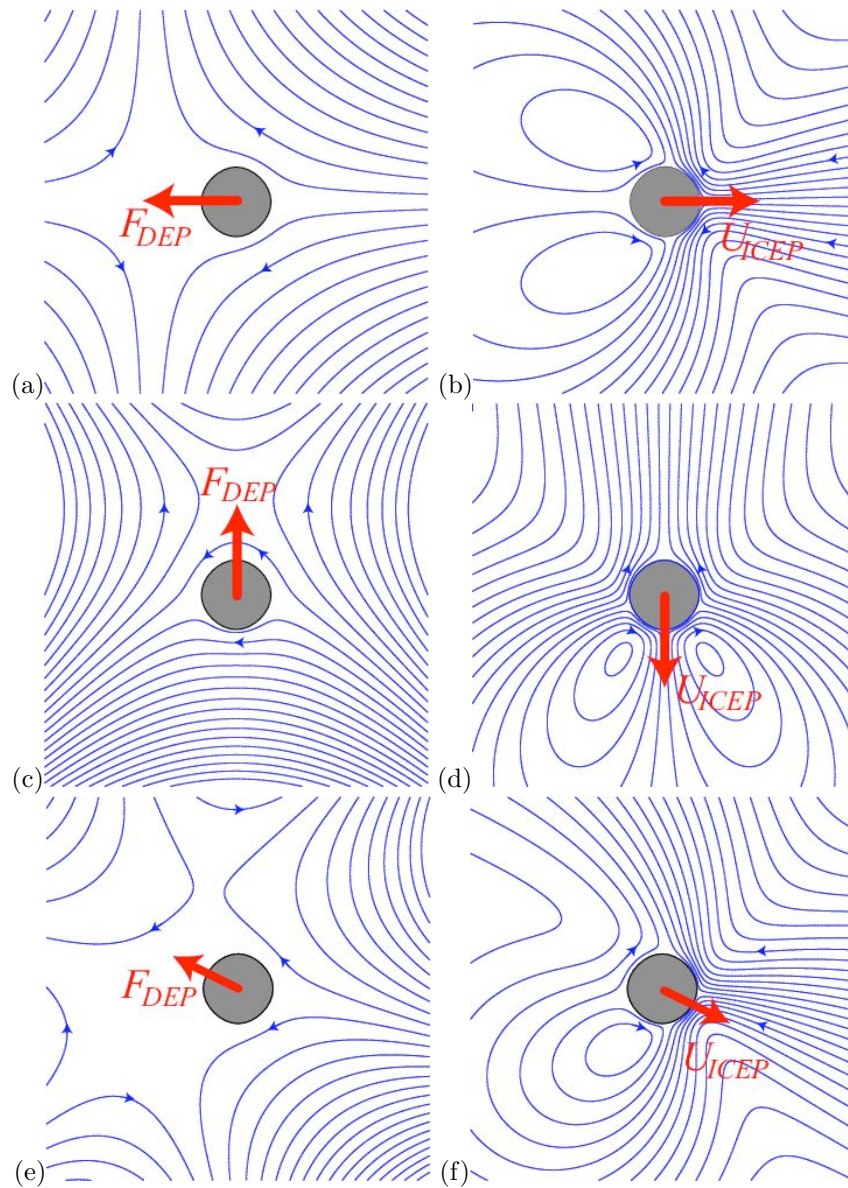


Figure 16. Analytical solutions of the Standard Model for diplophoresis in two dimensions. Electric fields (a,c,e) and ICEO flows (b,d,f) are shown around ideally polarizable cylinders in inhomogeneous elds. Regardless of the complexity of the multipolar background electric field distribution, the DEP force and ICEO velocity are always in opposite directions, as indicated. (Adapted from Squires and Bazant (2006).)

8 Electrophoresis of heterogeneous particles

In the previous section, we considered homogeneous polarizable particles, allowing for broken symmetries in the particle shape, which lead to induced-charge electrophoretic motion. In this section, we also allow for nonuniform surface properties. In order to appreciate the nonlinear effects of ICEP due to variable polarizability, we first review the possible types of linear response of heterogeneous particles with fixed surface charge.

8.1 Linear electrophoresis

The electrokinetic motion of colloidal particles and molecules in solution in response to applied electric fields can be rather complicated, so many approximations have been made in theoretical treatments. The classical theory of electrophoresis, dating back over a century to Smoluchowski, considers homogeneous particles, which are (i) non-polarizable, (ii) spherical, (iii) uniformly charged, (iv) rigid, (v) much larger than the thickness of the electrical double layer, (vi) in an unbounded fluid, very far from any walls or other particles, and subjected to (vii) uniform and (viii) weak fields, applying not much more than the thermal voltage ($kT/e=25\text{mV}$) across the particle in (ix) dilute electrolytes. Under these assumptions, the particles velocity is linear in the applied electric field, $\mathbf{U} = \mu_{ep}\mathbf{E}$, where the electrophoretic mobility, $\mu_{ep} = \varepsilon\zeta/\eta$, as noted above. In Smoluchowski's theory, the zeta potential is equal to the voltage across the double layer, which is proportional to the surface charge at low voltage.

Much less attention has been paid to the electrokinetic motion of heterogeneous particles, which have non-spherical shape and/or non-uniform physical properties. By far the most theoretical work has addressed the case linear electrophoresis of non-polarizable particles with a fixed, equilibrium distribution of surface charge (Anderson, 1989). Some examples are shown in Figures 17 and 18. In that case, relaxing only assumption (ii) leads to the classical prediction that the mobility of a particle of uniform composition (uniform zeta) is independent of the shape and size of the particle. Perhaps it was this insensitivity to geometry that led to the common belief that the electrophoretic mobility measures some kind of average surface charge, until Anderson (1984) was the first to clearly point out that this is generally not the case. By carefully relaxing only assumption (iii), he predicted that a sphere of non-uniform zeta potential can move in a different direction from the field and that its mobility is not simply related to its total charge. Generalizing work of Fair and Anderson (1992) on doublet particles, Long and Ajdari (1998) showed that relaxing both (ii) and (iii) leads to even more complicated behaviour, including particles that rotate

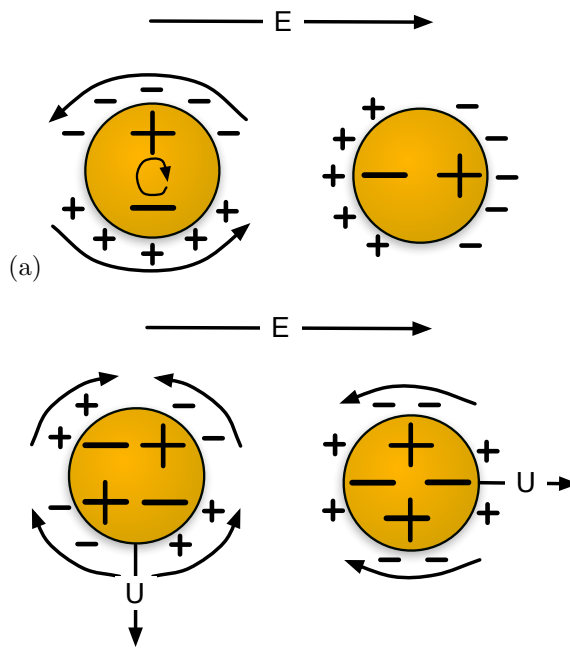


Figure 17. Linear electrophoretic motion of spherical heterogeneous particles with non-uniform fixed surface charge and thin double layers. (a) A dipolar charge distribution will rotate to align its dipole with the field, driven by both electrostatic torque and electro-osmotic flows (indicated). (b) A quadrupolar charge distribution can translate either perpendicular or parallel to the electric field, depending on its orientation.

continuously or translate perpendicular to a uniform DC field. Relaxing assumption (iv), the electrophoresis of flexible heterogeneous particles has also been studied, such as DNA molecules connected to beads (Long and Ajdari, 1996).

It is tempting to think of the electrophoretic mobility of a heterogeneous particle as a measure of its average charge, when in fact it has a nontrivial dependence on the spatial distribution of surface charge. This is clearly demonstrated by a counter-example of Long and Ajdari (1996), motivated by chain-like polyelectrolytes, such as DNA molecules. Consider a dumbbell-shaped particle consisting of two uniformly charged spheres with electrophoretic mobilities μ_1 and μ_2 and hydrodynamic drag coefficients ξ_1

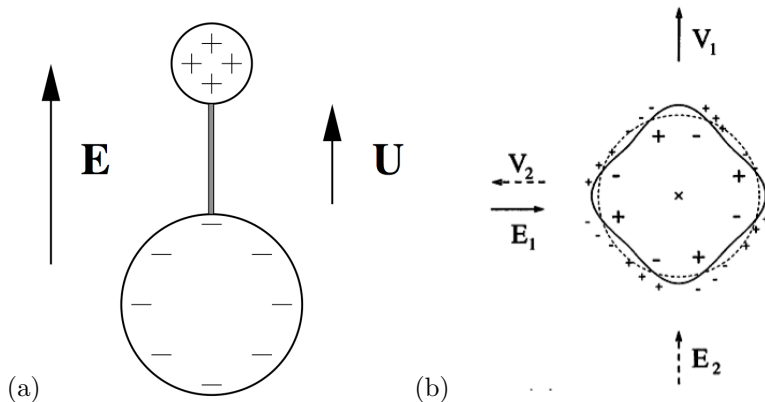


Figure 18. Examples of unusual linear electrophoretic motion of heterogeneous particles with asymmetric shapes. (a) A dumbbell consisting of two oppositely charged spheres of connected by a rigid rod rotates to align as shown and moves in the direction of the electric field (positive mobility), even though the total charge is negative, if the positive sphere is smaller. (b) A particle of zero total charge with four-fold and eight-fold perturbations in shape and surface charge, respectively, moves perpendicular to the electric field, regardless of its orientation (Adapted from Long and Ajdari (1998).)

and ξ_2 , held together by an uncharged, rigid rod. As a first approximation, the rod has negligible drag and is long enough that hydrodynamic and electrostatic interactions between the spheres can be neglected. In a uniform electric field, the dumbbell rotates to a stable configuration aligned with the field axis, as shown in Figure 18(a) and moves a velocity, $\mathbf{U} = \mu_{ep}\mathbf{E}$, where μ_{ep} is the overall mobility. In order for each particle ($i = 1, 2$) to move at the same velocity, the rod must exert a force, $\mathbf{F}_i = \xi_i(\mathbf{U} - \mu_i\mathbf{E})$. Force balance on the rod, $\mathbf{F}_1 = -\mathbf{F}_2$, then yields the mobility

$$\mu_{ep} = \frac{\xi_1\mu_1 + \xi_2\mu_2}{\xi_1 + \xi_2} \propto \frac{Q_1}{R_1} + \frac{Q_2}{R_2} \quad (51)$$

which is the drag-weighted average of the two mobilities. In the last step, we have used Stokes formula, $\xi_i = 6\pi\eta R_i$, and assumed that the local mobility (slip coefficient) is proportional to the surface charge density, $\mu_i \propto Q_i/4\pi R_i^2$, where Q_i is the total charge of each sphere. We see that, depending on the geometry, the mobility can have either sign, regardless of the sign the total

charge, $Q_1 + Q_2$. For example, as shown in Fig. 18(a), a small sphere of charge $Q > 0$ connected to a larger sphere of charge $-2Q$ can have a positive mobility, even though its total charge is negative, as long as $R_2 > 2R_1$.

Variations in charge density and shape can lead to even more surprising transverse electrophoretic motion, which departs from the field axis. In linear electrophoresis, a spherical particle of non-uniform surface charge (or zeta potential) can move perpendicular to the field, but only for certain orientations; it can also rotate, but only transiently to align its dipole with the field axis. These behaviors are shown in Fig. 17. If both the surface charge and the shape are perturbed, however, then these restrictions do not apply, as noted by Long and Ajdari (1998). Figure 18(b) shows a cylindrical particle of zero total charge, which always moves perpendicular to the electric field, regardless of its orientation. It has four-fold shape perturbation and eight-fold surface charge perturbation, such that each bump on the surface has positive surface charge to the left and negative to the right. By constructing appropriate chiral perturbations of the shape and surface charge, it is also possible to design heterogeneous particles, which rotate continuously around a particular axis without translating, for a particular direction of the electric field.

8.2 Induced-charge electrophoresis

The preceding examples involve non-polarizable objects with fixed surface charge distributions, which do not respond to the electric field. The resulting electrophoretic motion is linear in the field amplitude and vanishes for AC fields. The electrokinetic motion of polarizable particles, however, has nonlinear field dependence due to the phenomenon of induced-charge electro-osmosis (ICEO), where the field acts on induced diffuse charge in the electrical double layer. At frequencies low enough for capacitive charging of the double layer (typically < 10 kHz), the time-averaged motion in an AC field resembles that in a DC field. In the canonical example of an uncharged metal sphere in a uniform field, the ICEO flow is quadrupolar, drawing in fluid along the field axis and expelling it radially, but there is no net motion.

Motivated by the examples from linear electrophoresis above, Bazant and Squires (2004) pointed out that broken symmetry in ICEO flow generally causes particle motion, and coined the term, induced-charge electrophoresis (ICEP). Examples of broken symmetries include particles with irregular shapes and/or non-uniform physical characteristics, as well as non-uniform applied fields. In the latter case, ICEP occurs at the same time as dielectrophoresis (DEP), although the combined effects of ICEP and DEP on

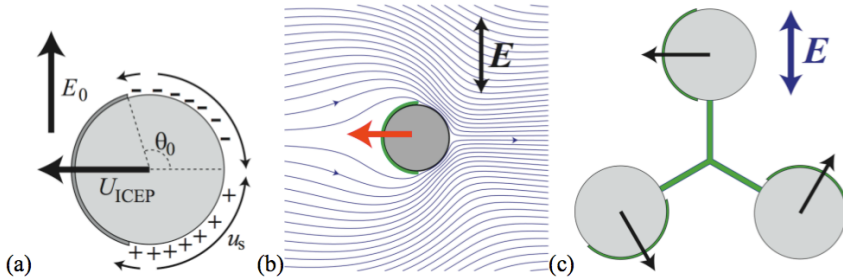


Figure 19. Induced-charge electrophoresis of Janus particles, illustrated for the case of metal partially coated with insulating thin films [from (9)]. (a) Stable orientation in a uniform field, showing induced charge and slip velocities on the metallic side, resulting in motion toward the insulating end, perpendicular to the field. (b) Streamlines of ICEO flow. (c) An ICEP pinwheel, consisting of three Janus particles connected by rigid rods, which tilts to align and then spins continuous around the field axis.

heterogeneous particles remain to be explored. Besides persisting in AC fields, ICEP also depends much more sensitively on particle shape and surface properties than does linear DC electrophoresis. Cases of non-spherical particles with uniform polarizability are discussed above, so we now focus on ICEP due to heterogenous surface polarizability.

The canonical example of Squires and Bazant (2006) is that of a Janus particle with one metallic and one insulating hemisphere, using the standard low-voltage model for electrokinetic motion of polarizable particles. In response to an applied electric field, the Janus particle rotates to align the interface between the two hemispheres with the field axis, due to both ICEP (electrohydrodynamics) and DEP (electrostatics). At the same time, for any orientation, the particle translates in the direction of its insulating end, propelled by ICEO flow on the metallic end, with a velocity

$$U = \frac{9\varepsilon\Lambda RE^2}{64\eta} \quad (52)$$

In particular, once the particle aligns in the field, it continues to move perpendicular to the electric field, with an azimuthal angle set by its initial orientation.

All the generic features of the dynamics still hold if the particles insulating end is smaller or larger than the metallic end, since it is determined by

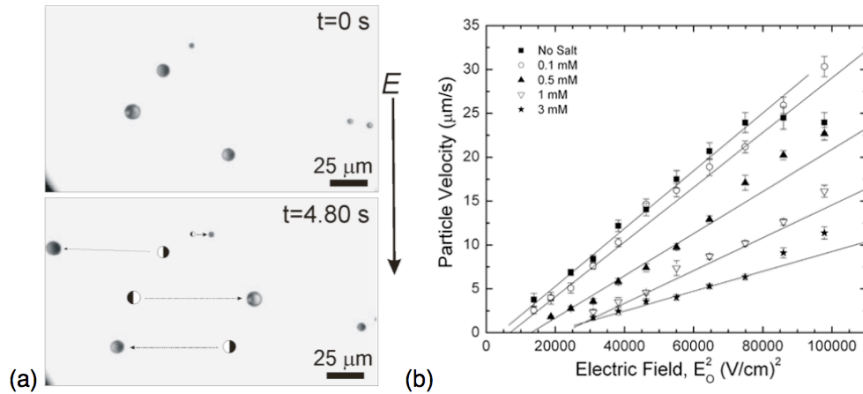


Figure 20. Experimental observation of induced-charge electrophoresis of metallo-dielectric Janus particles in a uniform 10 kHz AC field. (a) Sequence of micrographs demonstrating motion transverse to the field in the direction of the dielectric (light) end propelled by the metallic (dark) end, where the velocity increases with the particle size as in Eq. (52). (b) Velocity versus field amplitude squared at different bulk concentrations of NaCl. (Adapted from Gangwal et al. (2008).)

the broken symmetry. Motion transverse to a uniform AC field cannot have any contribution from DEP, but it is easily understood by considering the ICEO flow in Figure 19(a). After alignment in the field, part of the usual quadrupolar ICEO flow is suppressed on the insulating end. The remaining ICEO flow over the metallic end sucks in fluid along the field axis and pushes it outward from the metallic pole, as shown in Figure 19(b), which propels the particle toward the insulating pole.

This example suggests how to design particles that spin continuously in a uniform field, as noted by Squires and Bazant (2006). Since a Janus particle always translates towards its less polarizable end, a set of three Janus particles connected by rigid rods can be set into continuous motion like a pinwheel, if connected as shown in Figure 19(c). This ICEP pinwheel responds to any DC or AC electric field (of sufficiently low frequency) by tilting to align the particle plane perpendicular to the field and then spinning around the field axis until the field is turned off. Perhaps such particles could be used to sense electric fields or to apply torques to attached molecules or cells.

Transverse ICEP motion of metallo-dielectric Janus particles in a uni-

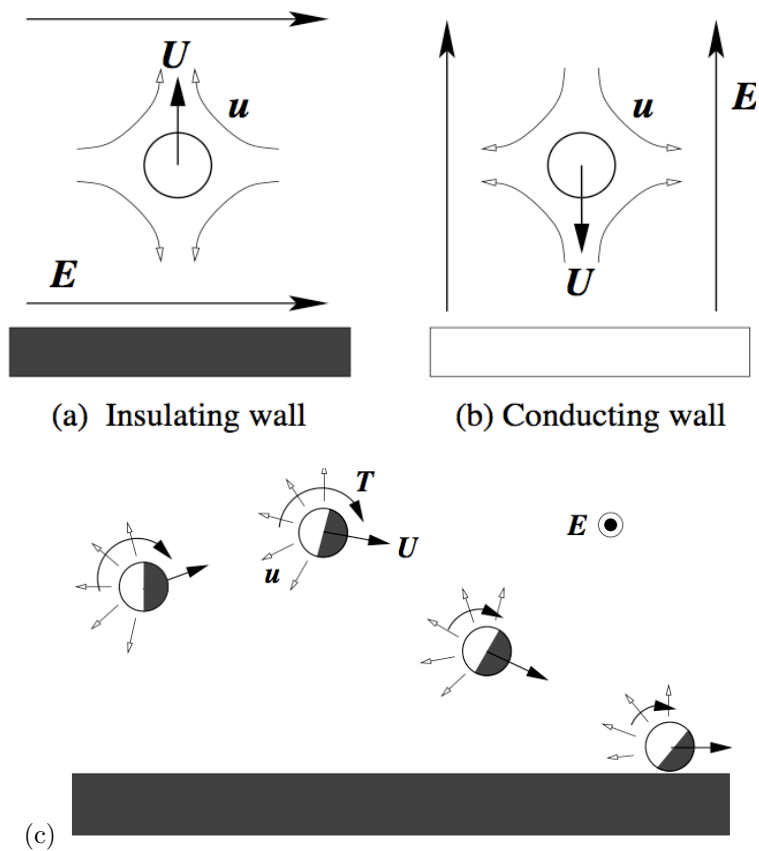


Figure 21. Wall interactions in induced-charge electrophoresis. Dominant hydrodynamic interactions between a homogeneous ideally polarizable particle and (a) an insulating wall and (b) an unscreened, ideally polarizable wall in a parallel electric field. (c) Theory by Kilic and Bazant (2007) of the interaction of a metallo-dielectric Janus particle and a insulating wall, as in the experiments of Gangwal et al. (2008). The particle rotates to align its equatorial plane with the field, with an arbitrary azimuthal angle. A steady ICEO flow sucks in fluid along the field axis (perpendicular to the page) and ejects it radially on the metallic side, which causes the particle to rotate to face the wall, due to a (mostly) hydrodynamic torque T . Near the wall, electrostatic torque can balance the viscous torque to enable motion parallel to the surface without contact, while maintaining a steady tilt angle. (Adapted from Kilic and Bazant (2007).)

form AC field has recently been observed by Gangwal et al. (2008). Consistent with theoretical predictions in Figure 19, the particles align and translate perpendicular to the field in the direction of the less polarizable (light) end, as shown in Figure 20. Larger particles move faster than smaller ones, as expected from Eq. (52), and the velocity scales like the field squared in dilute NaCl solutions. The ICEP velocity decays at higher concentrations, extrapolating to zero around 10 mM. The same concentration dependence is also observed in AC electro-osmotic flow and other nonlinear electrokinetic phenomena, which, although poorly understood, further reinforces that the motion is indeed due to ICEP.

Current research is focusing on how heterogeneous particles undergoing electrokinetic motion due to ICEP and DEP interact with walls and other particles. An interesting feature of the experiments in Gangwal et al. (2008) is that the Janus particles are attracted to nearby glass walls, and the transverse motion is also observed close to the walls, where the theory of Squires and Bazant (2006) does not strictly apply. This behavior is perhaps surprising because, according to the Standard Model, homogeneous particles should be repelled from insulating walls (and attracted to polarizable walls) by ICEO flows (Zhao and Bau, 2007a). Kilic and Bazant (2007) show that this attraction can be understood as a consequence of ICEP torque, which redirects the Janus particle toward a nearby wall and causes it to tilt while translating transverse to the field, as shown in Fig. 21

A major motivation to develop this subject is the possibility of new applications, opened by advances in microfluidics and nanotechnology. In principle, heterogeneous particles of specific irregular shapes and non-uniform electrical and/or chemical properties can be designed and fabricated for specific applications. The complex electrokinetic motion of these particles could potentially be used for separation or sample concentration in chemical or biological assays, self-assembly in the fabrication of anisotropic materials, directional transport of attached cargo, electric-field sensing and applying forces and torques to molecules or cells.

9 Induced-charge electro-osmotic mixing

Bazant and Squires (2004) proposed the use of ICEO flow around metallic microstructures (posts, surface patterns, etc.) for microfluidic mixing, switching, and pumping. The potential advantages of such elements in a microfluidic system include low power, programmability, and local flow control. As shown in Fig. 22, the basic physics of ICEO flow immediately suggests a number of designs involving metal posts or surface structures placed in microchannels with applied electric fields. Theoretical work using the Stan-

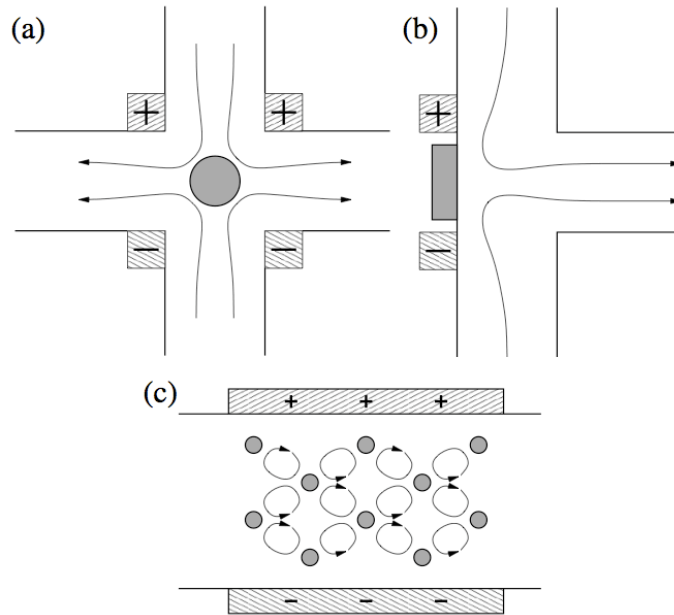


Figure 22. Simple microfluidic devices involving fixed metal posts or surface structures (shaded areas) driven by weak AC or DC fields applied at nearby microelectrodes (cross-hatched areas). Broken symmetries, such as triangular shapes, can lead to transverse flows, and sharp corners can enhance local ICEO flows in electrokinetic jets. (Reproduced from Bazant and Squires (2004).)

dard Model has shown that ICEO-based micro-mixing can be enhanced by broken symmetries (Squires and Bazant, 2006) or by the introduction of sharp corners in dielectric channel side walls (Yossifon et al., 2006).

In order to achieve rapid, programmable mixing of the fluid and any suspended particles, temporal modulation of the applied field can be used to produce *chaotic streamlines* (Zhao and Bau, 2007b). This concept is illustrated in Fig. 23. The basic idea is to switch between different asymmetric patterns to produce chaotic trajectories. Even if the underlying flows, $\mathbf{u}(\mathbf{r}, t)$, satisfy the linear Stokes equations and can be superimposed, the trajectories of passive tracer particles, $\mathbf{r}_i(t)$, generally satisfy a nonlinear

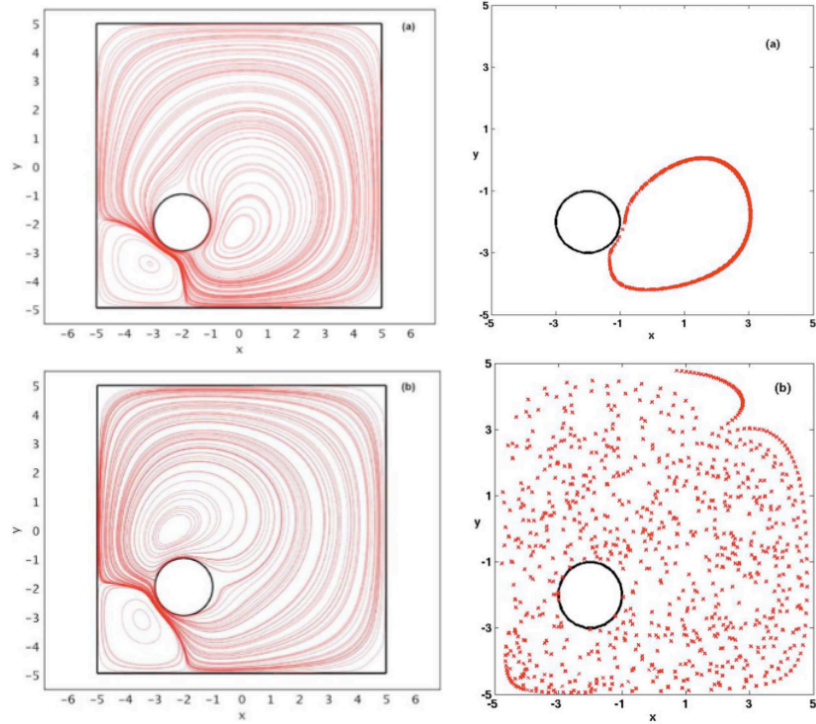


Figure 23. Simulation of an ICEO chaotic mixer with four electrodes on the side walls of a chamber (not shown) driving time-dependent ICEO flows around an off-center metal post. Left: by applying the field either north-south (top) or east-west (bottom), two different flows can be generated. Right: by alternating between these flows, chaotic advection be achieved, as evidenced by the stroboscopic plots (Poincaré section) of a particle, showing the transition from a nearly periodic loop (top) to a chaotic streamline (bottom) with increasing time. (Adapted from Zhao and Bau (2007a).)

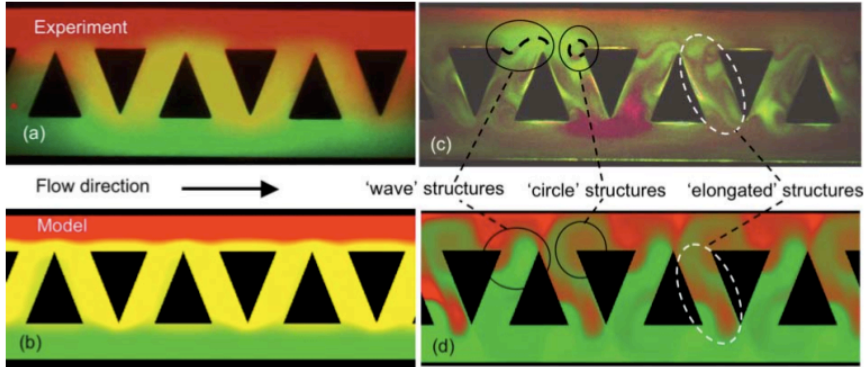


Figure 24. Experimental observation of induced-charge electro-osmotic mixing by Harnett et al. (2008), consistent with the theoretical predictions of Bazant and Squires (2004), sketched in Fig. 22c. Two colored fluid streams of 0.1 mM KCl flowing at 0.1 $\mu\text{l}/\text{min}$ from left to right undergo convective mixing by an array of asymmetric metal posts in a transverse AC field (6 Vpp, 100 Hz applied by electrodes above and below, separated by the channel width $200\mu\text{m}$). Images from experiments (a,c) and simulations of advection-diffusion in ICEO flow in the same geometry (b,d) show the distribution of red and green fluorescent beads after loading (a,b) and during mixing (c,d). (Reproduced from Harnett et al. (2008))

ordinary differential equation,

$$\frac{d\mathbf{r}_i}{dt} = \mathbf{u}(\mathbf{r}_i(t), t) \quad (53)$$

which can have chaotic solutions, suitable for mixing. The same principle of chaotic advection was originally developed for passive microfluidic mixing by pressure-driven flows in grooved channels (Stone et al., 2004).

The first microfluidic demonstration of ICEO flow around a metal cylinder by Levitan et al. (2005) showed steady vortices, but did not study mixing. In 2008, two groups reported the first experimental demonstrations of microfluidic mixing by ICEO flow around metallic microstructures, effectively reducing to practice the theoretical predictions of Ref. Bazant and Squires (2004). (i) Harnett et al. Harnett et al. (2008) integrated an array of gold-coated posts of triangular cross section in a microchannel with electrodes applying a low-frequency AC field on the side walls, as shown in Fig. 24. The post-array mixer was placed at the junction of

two Y-channels, and programmable on/off mixing of two different streams of dilute electrolytes was demonstrated. Good agreement with theoretical predictions was noted, albeit with a correction factor of $\Lambda = 0.25$. (ii) Wu and Li (2008b,a) reported simulations and experiments on ICEO mixing in flow past pointed platinum “hurdles” (floating electrodes) and different geometrical designs were compared. Further design improvements could benefit from numerical optimization methods for ICEO flows developed by Gregersen et al. (2009).

ICEO mixers can be used to enhance the transport of slowly diffusing molecules to an active surface. In biomedical microfluidics, ICEO flows can improve the sensitivity biological assays by passing probe molecules, such as DNA or proteins, rapidly over a detection surface. In electrochemical systems for water purification and desalination, ICEO mixers can enhance the transport of salt and impurities to a membrane or porous electrode for rapid removal, beyond diffusion limitation.

10 AC electro-osmotic pumping

10.1 Slip-driven microfluidic pumps

There are many strategies for microfluidic pumping, as reviewed by Laser and Santiago (2004), Stone et al. (2004), Squires and Quake (2005). Pumps based on fluid body forces, due to externally applied pressure gradients, magnetic fields, electrothermal forces, etc., lose their efficiency with miniaturization, due the overwhelming viscous drag at no-slip walls. On the other other hand, the same viscous drag can be put to use in pumps that generate flow by effective fluid slip on the walls, which only get more efficient with miniaturization. This is the principle behind all electro-osmotic micropumps, whether linear or nonlinear in the applied voltage.

The basic physics of slip-driven pumping are illustrated in Figure 25. For any pump operating in the viscous regime of low- Reynolds number, the flow rate decays linearly with the back pressure P according to

$$\frac{Q}{Q_{max}} = 1 - \frac{P}{P_{max}} \quad (54)$$

where Q_{max} is the flow rate at $P = 0$ and P_{max} is the back pressure that yields $Q = 0$ and effectively stops the pump. By linearity, whenever the pump operates against a hydraulic resistance, the slip-driven flow in the forward direction is superimposed with a pressure-driven parabolic Poiseuille flow profile in the opposite direction. The situation can be modeled by an equivalent electrical circuit shown in the Figure 25, where the pump consists of constant current Q_{max} in parallel with the back-flow resistance R_B .

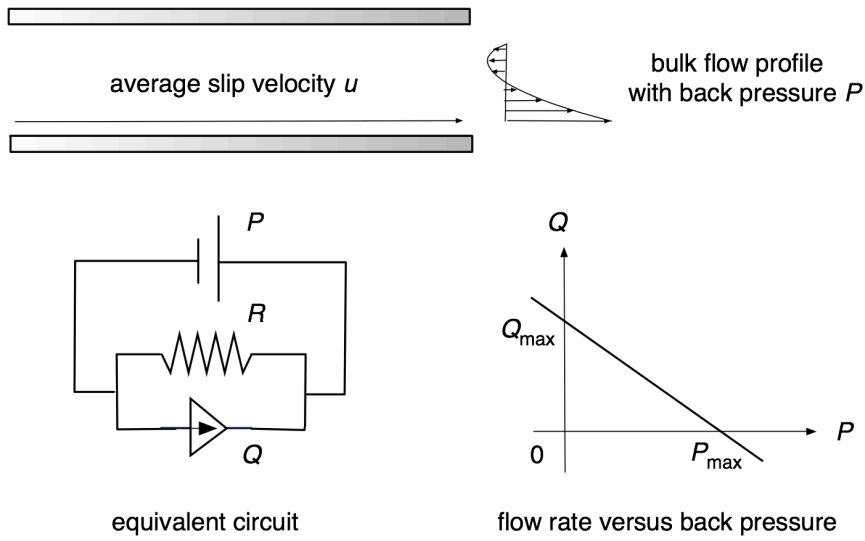


Figure 25. Basic physics of slip-driven micropumps. The pump generates a flow rate Q in a microchannel driven by fluid slip over a wall. If the pump encounters a back pressure drop P , driving a back-flow through its hydraulic resistance R , the net flow is given by the linear relation, $Q - PR$. The maximum flow rate (at $P = 0$) is $Q_{max} = Q$, while the maximum back-pressure which stops the pump ($Q = 0$) is $P_{max} = Q/R$.

To estimate these quantities, consider a microchannel of rectangular cross section with a wide floor of width W producing slip and a much smaller height $H \ll W$, and solve for the resulting Stokes flow. The total flow rate due to a mean slip velocity U over the bottom surface is

$$Q_{max} = \frac{\alpha HWU}{2} \quad (55)$$

where $\alpha \sim 1 - (1/2)(H/W)^2$ corrects for fringe flows in the limit $H \ll W$. The back pressure required to stop the net forward flow is given by

$$P_{max} = R_B Q_{max} = \frac{UL}{k} = \frac{6\eta\alpha UL}{H^2} \left[1 + \left(\frac{H}{W} \right)^2 \right] \quad (56)$$

k is the hydrodynamic Darcy permeability and L is the length of the microchannel.

10.2 DC versus AC electro-osmotic pumps

This simple calculation shows that the hydraulic resistance to back flow, and thus P_{max} , can be increased by reducing the micro-channel height H . This strategy has been used to boost the pressure of DC electro-osmotic pumps by employing linear electro-osmotic flows in porous glass frits with submicron pores (Yao and Santiago, 2003). Electro-osmotic micropumps can achieve large head pressures, exceeding 50 atm, without any moving parts, but they require large DC voltages up to kilo-Volts. Such large voltages cause Faradaic reactions, such as water electrolysis, leading to hydrogen and oxygen gas production at the electrodes, which must be managed carefully.

The large operating voltage and the need to manage reaction products can hinder the application of DC electro-osmotic pumps in portable or implantable lab-on-a-chip devices. Moreover, it is difficult to locally manipulate the fluid within the microchannels by applying an electric field across the entire device. These drawbacks can be overcome using small AC voltages applied at microelectrodes suitably distributed inside a microfluidic system. The integration of electrodes in the channel limits the extent to which the channel height H can be reduced, but useful pressures can still be generated using small AC applied voltages, around 1 Volt (root mean square), with greatly reduced Faradaic reactions.

As described above, classical electrokinetic phenomena are linear in the applied voltage and thus cannot produce any net flow under alternating current conditions. A variety of nonlinear electrokinetic phenomena, which persist in AC fields, have been known for decades in colloid science, but the focus has been on electrophoretic mobility and particle interactions. The advent of microfluidics has stimulated interest in the use of electric fields to drive fluid flows, without any moving parts. In this context, nonlinear electrokinetics offers some unique advantages, such as the reduction of unwanted electrochemical reactions (using AC voltages) and the ability to drive fast, programmable flows at low voltages (using closely spaced micro-electrodes).

This area of research in nonlinear electrokinetics began with the discovery of Ramos et al. (1999) of steady electro-osmotic flow over a pair of micro-electrodes applying an AC voltage and dubbed the effect AC electro-osmosis. Around the same time, Ajdari (2000) predicted ACEO flow over periodic electrode arrays and showed how the effect could be used for long-range pumping. As the performance of ACEO pumps has advanced (Huang et al., 2010), ACEO has also been exploited, in conjunction with dielectrophoresis in different geometries to manipulate particles and cells in microfluidic devices (Green et al., 2000b; Wong et al., 2004; Wu, 2006).

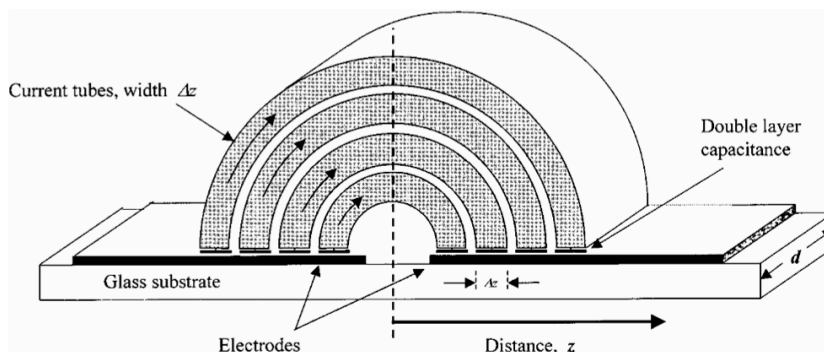


Figure 26. Equivalent RC circuit model for double-layer charging over a pair of electrodes. The inner edges of the electrodes encounter less bulk resistance (due to shorter current tubes) and thus charge more quickly than the outer edges. (Reproduced from Ramos et al. (1999).)

10.3 Flows over ideally polarizable electrodes

ACEO is a phenomenon of induced-charge electro-osmosis, where flow is generated by the action of an electric field on its own induced diffuse charge near a polarizable surface. The main difference with other examples of ICEO flows discussed above is that ACEO involves electrode surfaces, which supply both the electric field and the induced screening charge, in different regions at different times. For this reason, ACEO is inherently time-dependent (as the name implies) and tied to the dynamics of diffuse charge, as ions move to screen the electrodes.

Perhaps the easiest way to understand ACEO is to consider a pair of ideally polarizable planar electrodes applying a sudden DC voltage (which is analogous to ICEO flow around a polarizable particle in a sudden electric field). As shown in Figure 26, charge relaxation can initially be described by an equivalent RC circuit, where the diffuse layers act as capacitors, connected to current tube resistors of varying length through the bulk solution. Since the resistance is smaller (and the field larger) near the gap, the inner portions of double layers on the electrodes charge more quickly than the outer portions. As shown in Figure 27, this causes ICEO flow to occur, directed outward from the gap, only when the electrodes are partially screened, as the tangential field from the unscreened outer portions acts on induced charge on the inner portions. Note that the flow is independent of

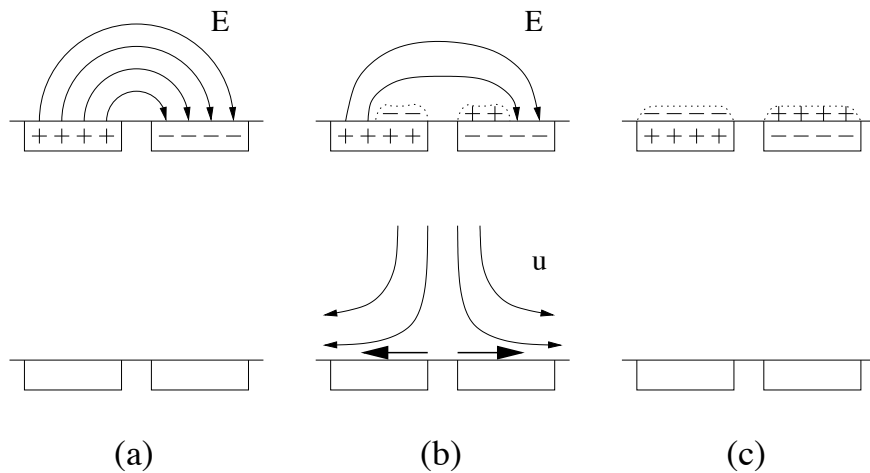


Figure 27. The basic physics of AC electro-osmosis. Electrochemical relaxation (top) and induced - charge electro-osmotic flow (bottom) in response to a suddenly applied voltage across an electrode pair. (a) At first the electric field has no tangential component on the electrodes, since they are equipotential surfaces, and thus there is no electro-osmotic flow. (b) Capacitive double-layer charging begins near the gap where the initial normal current is strongest and causes the unscreened field lines dip down and provide tangential components over the induced charge; the result is ICEO flow directed away from the electrode gap. (c) After the charging time passes, the electrodes are fully screened, leaving no electric field and thus no flow. An AC voltage can drive a steady time-averaged flow, similar to (b), if its period is comparable to the charging time. (Reproduced from Bazant (2008a).)

the sign of the applied voltage: If the polarity were reversed, then the field and induced charges would both change sign, resulting in the same ICEO flow.

Under AC forcing, the flow peaks when the oscillation period is comparable to the charging time (Fig. 27b). ACEO flow decays at higher frequencies, since there is not enough time for charge relaxation (Fig. 27a). It also decays at lower frequencies, since there is enough time to completely screen the bulk electric field (Fig. 27c).

The theory of ACEO is mostly based on the Standard Model using the complex potential for AC forcing, following González et al. (2000) as described in Section 6. In this regime, the basic scaling of time-averaged ACEO flow is

$$\langle u \rangle \sim \frac{\Lambda(\omega/\omega_c)^2}{[1 + (\omega/\omega_c)^2]^2} \frac{\varepsilon V^2}{\eta L} \quad (57)$$

where V is the applied voltage amplitude and L is electrode spacing (roughly from center to center). The basic velocity scale for ACEO is the same as the electroviscous scale u_0 for ICEO flow with the characteristic field, $E \sim V/L$, and induction length $R = L$. The frequency-dependent prefactor is a Lorentzian spectrum peaking at the critical frequency,

$$\omega_c \sim \frac{D}{\lambda_D L} \frac{C_D}{C} \quad (58)$$

which is the inverse of the RC time scale τ defined above.

10.4 Fluid pumping by micro-electrode arrays

Some useful general principles have been developed to guide the design of ACEO pumps. The flows discovered by Ramos et al. (1999) over small numbers of electrodes can be used for local fluid mixing or particle trapping at stagnation points, but the flow decays quickly away from the electrode surfaces. A symmetric, periodic array of many inter-digitated electrodes (of alternating polarity at each moment in time) similarly produces an array of counter-rotating convection rolls, but no net pumping of the fluid in one direction. Instead, long-range pumping over an electrode array requires *broken symmetry within each spatial period* to rectify the AC forcing.

There are several ways to design ACEO pumps by breaking symmetry in a periodic electrode array. Ajdari (2000) originally suggested modulating either the electrode capacitance via a dielectric coating (Figure 28a) or the surface height (Figure 28b) with half the spatial period of the array, so that the one side of each electrode drives stronger ACEO flow compared to the other side and thus wins to produce net pumping over the array. In the first

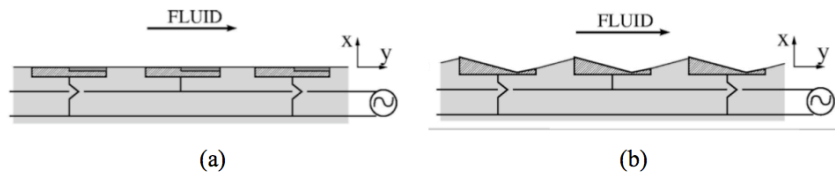


Figure 28. Sketches of local broken symmetries in a periodic electrode array which lead to global time-averaged ACEO pumping: (a) non-uniform surface coatings; (b) non-uniform surface height. (Reproduced from Ajdari (2000).)

implementation of an ACEO pump, Brown et al. (2000) opted instead to break symmetry by using planar electrodes of different widths and gaps, and, until recently, this design was the only one studied experimentally (Studer et al., 2004) or theoretically (Olesen et al., 2006). It has been shown to generate velocities over 100 microns/sec, although it also exhibits poorly understood flow reversals (see below).

The performance of ACEO pumps can be greatly enhanced by designing appropriate non-planar electrode geometries. As recently predicted by Bazant and Ben (2006), various 3D ACEO designs exhibit dramatically increased flow rate without flow reversal, due to a special geometry in which the non-uniform slip profile on the electrodes all contributes to flow in the same direction. The basic idea is to create a fluid conveyor belt with electrodes each having steps of two different heights: On each electrode, the region of desired forward flow is raised up, while the region of reverse flow is recessed below, so as to recirculate in a vortex aiding the forward flow (rather than fighting it, as in planar designs). This can be accomplished with electrodes having electroplated metal steps, as shown in Figure 29, although other designs are possible, such as flat electrode steps deposited on a grooved surface (without the vertical metal surfaces). Simulations predict that 3D ACEO pumps are faster than planar pumps by more than an order of magnitude, at the same voltage and minimum feature size, and thus can achieve mm/sec velocities with only a few volts. This suggests using 3D ACEO pumps to drive flows in battery-powered, portable or implantable microfluidic devices.

Huang et al. (2010) recently reported the state-of-the-art in 3D ACEO micropumps and demonstrated the first integration of ACEO (or ICEO) flow control in a portable biomedical lab-on-a-chip device (Fig. 30). Their de-

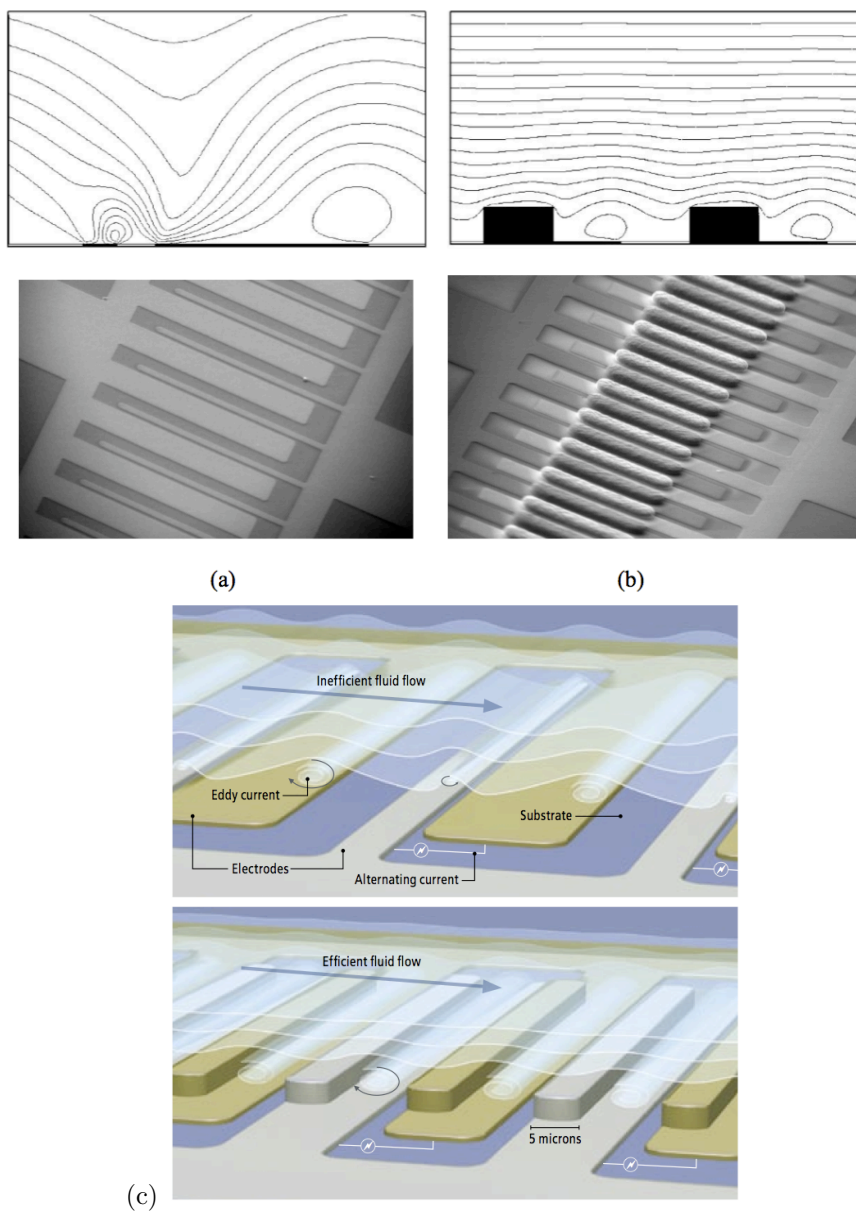


Figure 29. Top (a,b): Simulations of ACEO microfluidic pumps, showing the time-averaged flow over a pair of micro-electrodes (dark regions) in one spatial period of an interdigitated-electrode array. (a) A nearly optimal planar design with different electrode sizes and gaps; the smaller electrode has the largest local slip velocity, but the larger electrode wins in overall pumping from left to right. (b) A more efficient 3D ACEO design with stepped electrodes having a symmetric footprint and the same minimum feature size; the reverse slip now recirculates in a vortex to create a fluid conveyor belt for the raised pumping flow from left to right. (Reproduced from Bazant and Ben (2006)). Bottom (a,b): Scanning electron microscopy images of each design fabricated in gold on glass with minimum feature size (gap) of 5 microns. (Courtesy of J. P. Urbanski and J. A. Levitan, using methods of Urbanski et al. (2006b)). (c) Artist's rendering of these flows. (Reproduced from Choi (2007).)

sign is based on (i) theoretically optimal electrode shapes for ultrafast flows predicted by Burch and Bazant (2008) and (ii) long, serpentine microchannels to dramatically boost the head pressure, by an order of magnitude over previous devices. The latter effect takes advantage of the scaling of the head pressure with length, $P_{max} \sim L$, in Eq. (56). With 1.06 Volt (rms) applied at 1-10 kHz, the pump achieved pressures over 1% atm and mean velocities over 1 mm/sec in water, sufficient to drive flows for an on-chip DNA micro-array assay. The current (mA) and power consumption (mW) are easily provided by a small Li-ion battery, so this work opens new possibilities for portable or implantable microfluidic systems. As with other ICEO phenomena, however, ACEO pumps require dilute electrolytes, which may be a fundamental limitation (Bazant et al., 2009b).

Simple scaling arguments show how to design serpentine ACEO pumps with desired characteristics. The flow rate or pressure can be increased by connecting multiple pumps in parallel or in series, respectively. For example, since our prototype pump consists of only one thin layer (25 nm channels), its pressure can be increased by a factor of ten, exceeding 10% atm simply by stacking ten layers (for a total thickness below 1 mm). Regardless of the channel layout, for a given device volume, there is always trade-off between maximum flow rate and maximum pressure. We have already noted that to maximize pressure, the channel height, H , should be reduced as much as possible, given the electrode sizes and fabrication methods, so this should be viewed as a constant when designing the channel layout. To tune the flow rate, we can vary the channel width W .

Material and fabrication constraints limit the total device cross-sectional area per channel A , which includes the surrounding walls and substrate thickness, and is thus larger than the internal channel cross-sectional area HW . The fabrication method thus sets the ratio $\beta = HW/A$. For a given volume Ω , the total length of the channel can be estimated as $L = \Omega/A$, ignoring any corner effects in regions of the channel without a pumping surface. Using Eq. (56), we find

$$P_{max}Q_{max} = \beta\gamma\frac{U^2\Omega}{H^2} \quad (59)$$

where $\gamma < 1$ is a constant, reflecting the hydraulic resistance of corners and connections, compared to the pumping regions. For fixed velocity, volume, and channel height, we see that the maximum pressure is inversely proportional to the maximum flow rate. This formula also determines the required volume for the pump, given target specifications of flow rate and pressure for a given application.

Fluid pumping over electrode arrays can also be achieved by applying

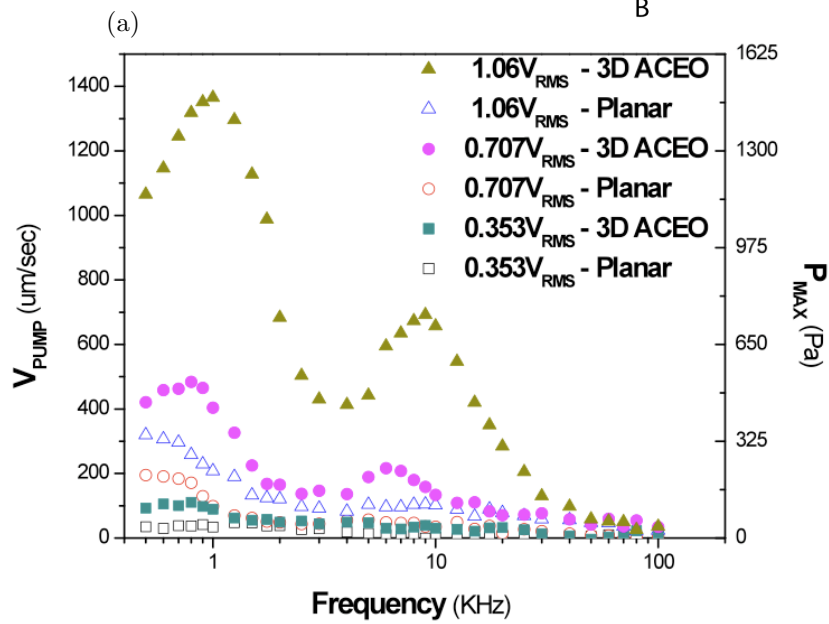
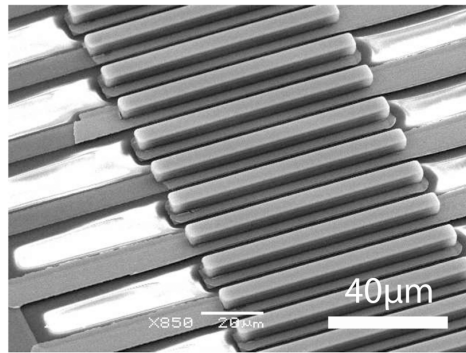
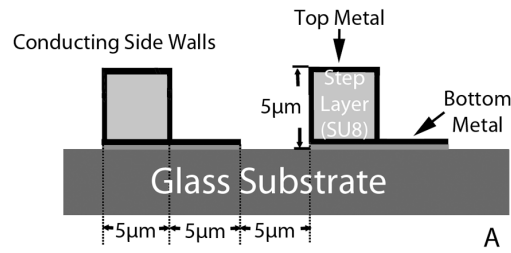


Figure 30. State-of-the-art ACEO micropumps by Huang et al. (2010), using theoretical predicted optimal electrode shapes to create a “fluid conveyor belt” . (a) Fabrication schematic and SEM image of a 3D stepped electrode array, close to the predicted optimal geometry. (b) Experimental demonstration of ultra-fast ($> 1 \text{ mm/sec}$) mean velocity over the pump for water in a microfluidic loop with 1.06 Volt rms (3 Vpp), outperforming the standard planar pump of Brown et al. (2000) shown below in Fig. 33(b). The head pressure ($> 1\% \text{ atm}$) is increased by an order of magnitude using long serpentine channels to hinder reverse pressure-driven flow. (Reproduced from Huang et al. (2010).)

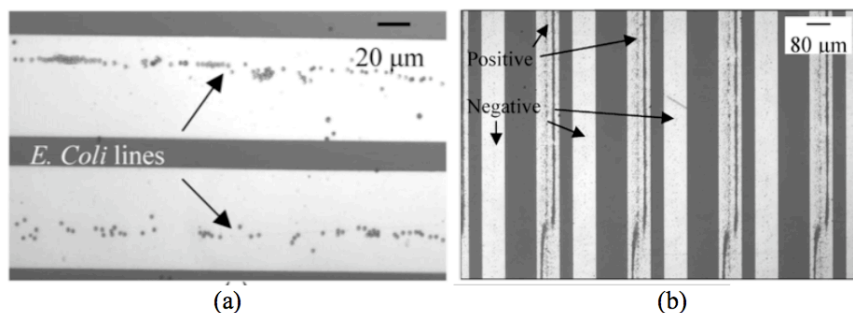


Figure 31. (a) Collection of *E. Coli* bacteria in tap water along the stagnation lines of ACEO flow on Au microelectrodes at low frequency (100 Hz) and moderate voltage (1 V). (b) Preferential particle trapping by asymmetric polarization ACEO on electrodes with positive DC bias at higher voltage (> 3 V). (Reproduced from Wu (2006).)

a traveling wave of voltage. At low frequency, a similar induced-charge electro-osmotic mechanism, which peaks at the RC frequency ω_c , is responsible for the flow (Cahill et al., 2004). At high frequency (or with a thick dielectric coating on the electrodes), the classical Erlich-Melcher effect used to pump dielectric liquids, which peaks at the Debye frequency, D/λ_D^2 , can also be observed (Ramos et al., 2005). Although traveling-wave ACEO seems to produce slower net flow than standing-wave ACEO with planar electrodes, the possibility of designing suitable non-planar electrodes has not yet been considered.

ACEO flows can also be used to manipulate colloidal particles and biological cells in microfluidic devices (Green et al., 2000b; Wong et al., 2004; Wu, 2006). The basic strategy is to use ACEO flow to draw particles to stagnation points on the electrodes, where they are trapped, presumably by DEP (although the classical theory does not seem to predict this effect). By increasing the voltage, the ACEO flow can be reversed, and particles are observed to move away from the stagnation lines, overcoming any remaining trapping force. In this way, it is possible to write and erase suspended particles, bacteria, or micro-algae on microelectrodes, as shown in figure 7(a). This effect can be enhanced by added a DC bias voltage to the low-frequency AC voltage (50-100 Hz) between adjacent electrodes, as proposed by Wu (2006). Particles are observed to collect only on the positively biased electrode, as shown in Figure 31(b). It has been suggested that opposing

ACEO flows are produced by the competition between Faradaic charging on one electrode (positive bias) and capacitive charging on the other (negative bias), but a quantitative theory remains to be developed.

11 Beyond the Standard Model

In spite of many successes, the Standard Model has some serious shortcomings, recently reviewed and analyzed by Bazant et al. (2009b). It generally over-predicts fluid velocities compared to experiments, sometimes by orders of magnitude. It also fails to capture key experimental trends, such as the decay of ICEO flow with increasing salt concentration, flow reversals at high voltage and/or high frequency, and ion-specificities. The reasons for these discrepancies are not yet fully understood.

Bazant and Squires (2010) have reviewed various recent theoretical advances, which extend the Standard Model in the following ways: (i) thin-double-layer approximations for large induced voltages based on the classical Poisson-Nernst-Planck (PNP) equations of ion transport and Navier-Stokes (NS) equations of fluid flow, (ii) thick-double-layer approximations for the PNP/NS equations at low voltages, (iii) modified boundary conditions for electrochemical processes, and (iv) modified PNP/NS equations for large voltages and/or concentrated solutions. The reader is referred to the review articles for details, and here we only mention one interesting new effect of the latter type, related to (solvated) ion crowding in highly charged double layers.

As shown in Fig. 32, when the surface potential relative to the bulk solution greatly exceeds the thermal voltage $k_B T/e$, ions inevitably become crowded in the inner portion of the double layer, and this pushes apart the diffuse screening cloud away from the surface, thus effectively separating the two plates of the double layer capacitor. Since capacitance is inversely proportional to the plate separation, the crowding of ions at high voltage causes the differential capacitance to decrease at large voltages, as the square root of the voltage, once a condensed layer of uniform charge density forms. In contrast, the classical Gouy-Chapman model of dilute-solution theory predicts the opposite voltage dependence, an exponential growth of capacitance with voltage, given by Eq. (29), since nothing stops point-like ions from piling up at the surface (or Outer Helmholtz Plane). Using a simple mean-field theory of excluded volume effects for finite-sized ions, Kilic

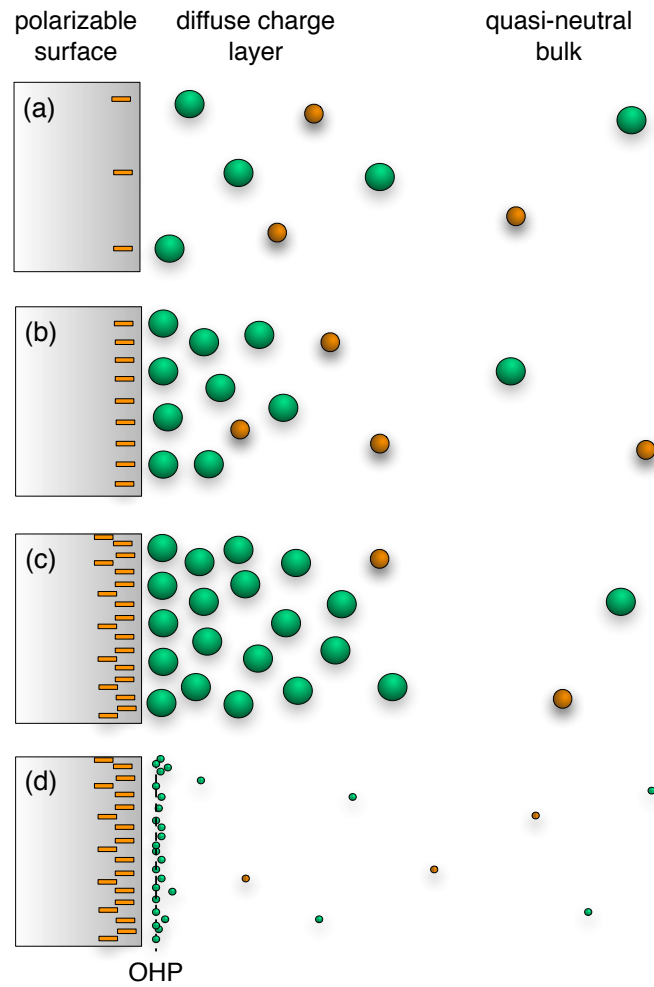


Figure 32. Solvated counterions (larger green spheres) and co-ions (smaller orange spheres) near a polarizable surface. (a) At small induced voltages, $\Psi_D \ll \Psi_c$, the neutral bulk is only slightly perturbed with a diffuse-charge layer of excess counterions at the scale of λ_D . (b) At moderate voltages, $\Psi_D \approx \Psi_c$, the diffuse layer contracts, as described by Poisson-Boltzmann (PB) theory. (c) At large voltages, $\Psi_D \gg \Psi_c$, the counterions inevitably become crowded, causing expansion of the diffuse layer compared to the predictions of the classical Gouy-Chapman-Stern model, sketched in (d), which is based Poisson-Boltzmann theory for point-like ions with a minimum distance of approach, the “outer Helmholtz plane” (OHP), to model solvation of the surface. (Reproduced from Bazant et al. (2009b).)

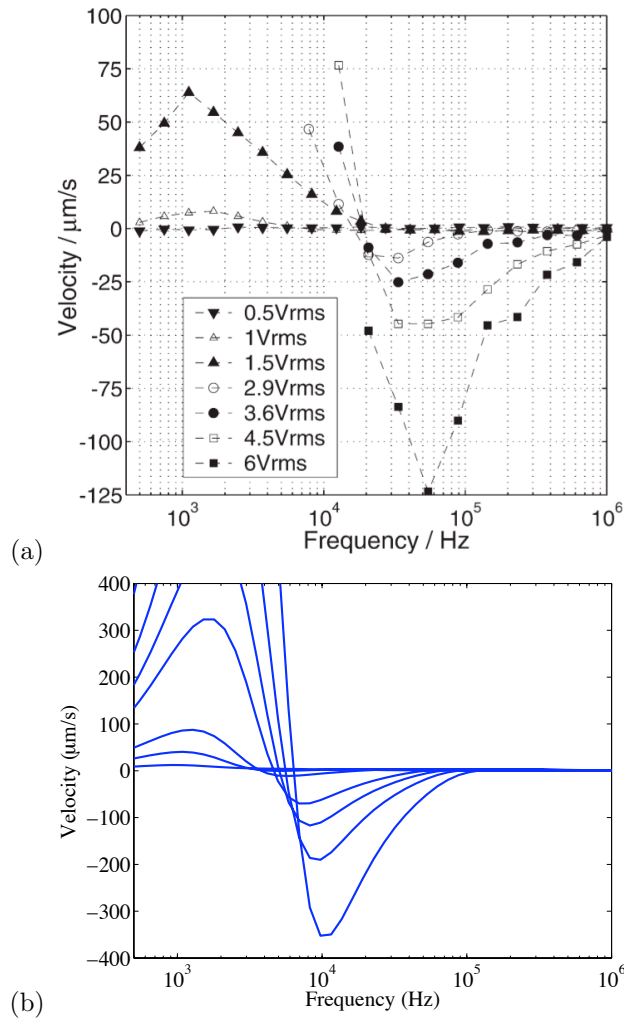


Figure 33. Crowding of finite-sized ions (Fig. 8) and high-frequency flow reversal of planar ACEO pumps. (a) Experimentally observed velocity pumping of 0.1mM KCl by the ACEO pump of Brown et al. (2000) around a microfluidic loop versus AC frequency at different peak-to-peak voltages (reproduced from Studer et al. (2004)). (b) Simulations of the same flow using a modified electrokinetic equations with an effective hydrated ion size $a = 4.4$ nm for a lattice gas in the mean-field local-density approximation; similar results are obtained using a solvated ion diameter $a \approx 1$ nm for hard spheres with dielectric saturation in water (reproduced from Storey et al. (2008)).

et al. (2007) derived a more general capacitance formula

$$C_D^\nu = \frac{\frac{\epsilon}{\lambda_D} \sinh\left(\frac{ze\Psi_D}{k_B T}\right)}{[1 + 2\nu \sinh^2\left(\frac{ze\Psi_D}{2k_B T}\right)] \sqrt{\frac{2}{\nu} [1 + 2\nu \sinh^2\left(\frac{ze\Psi_D}{2k_B T}\right)]}} \quad (60)$$

where $\nu = 2c_0/c_{max}$ is the bulk volume fraction of ions (in a binary electrolyte). Chapman's formula (29) is recovered in the dilute solution limit, $\nu \rightarrow 0$, or at low voltages. With this convenient analytical expression, Storey et al. (2008) were able to predict the flow reversal of ACEO pumps at high frequency and high voltage, in reasonable agreement with the experiments of Studer et al. (2004), as shown in Fig. 33. At high voltage and low frequency (or in the DC limit), Faradaic charge-transfer reactions consume normal current and can discharge the double layer, like a short circuit. At high frequency, however, the polarity of the double layer changes too quickly and solvated ions are squashed near the surface and then quickly removed, prior to the onset of Faradaic reactions.

12 Conclusion

Induced-charge electrokinetic phenomena comprise an active and growing, interdisciplinary field of research, which spans colloid science, microfluidics, and electrochemical systems. ICEO flows occur to some degree at any interface between an electrolyte and a polarizable surface, subject an applied voltage or electric field. With the advent of microfabrication techniques, ICEO flows can now be probed and exploited with high precision in microfluidic devices or designer colloidal particles. Beyond these engineering opportunities, induced-charge electrokinetic phenomena raise profound scientific questions about the structure and dynamics of highly-charge double layers.

Bibliography

- A. Ajdari. AC pumping of liquids. *Phys. Rev. E*, 61:R45–R48, 2000.
- J. L. Anderson. Effect of non-uniform zeta potential on particle movement in electric fields. *J. Colloid Interface Science*, 105:45–54, 1984.
- J. L. Anderson. Colloid transport by interfacial forces. *Annu. Rev. Fluid Mech.*, 21:61–99, 1989.
- N. O. Barinova, N. A. Mishchuk, and T. A. Nismeyanova. Electroosmosis at spherical and cylindrical metal surfaces. *Colloid Journal*, 70:695–702, 2008.

- E. Barsoukov and J. R. Macdonald, editors. *Impedance spectroscopy: Theory, experiment and applications*. J. Wiley & Sons, 2005.
- M. Z. Bazant. AC electro-osmotic flow. In D. Li, editor, *Encyclopedia of Microfluidics and Nanofluidics*, volume Part 1, pages 8–14. Springer, 2008a.
- M. Z. Bazant. Nonlinear electrokinetic phenomena. In D. Li, editor, *Encyclopedia of Microfluidics and Nanofluidics*, volume Part 14, pages 1461–1470. Springer, 2008b.
- M. Z. Bazant and Y. Ben. Theoretical prediction of fast 3d AC electro-osmotic pumps. *Lab on a Chip*, 6:1455–1461, 2006.
- M. Z. Bazant and T. M. Squires. Induced-charge electrokinetic phenomena. *Current Opinion in Colloid and Interface Science*, 15:203–213, 2010.
- M. Z. Bazant and T. M. Squires. Induced-charge electro-kinetic phenomena: Theory and microfluidic applications. *Phys. Rev. Lett.*, 92:066101, 2004.
- M. Z. Bazant, K. Thornton, and A. Ajdari. Diffuse charge dynamics in electrochemical systems. *Phys. Rev. E*, 70:021506, 2004.
- M. Z. Bazant, M. S. Kilic, B. D. Storey, and A. Ajdari. Nonlinear electrokinetics at large voltages. *New Journal of Physics*, 11:075016, 2009a.
- M. Z. Bazant, M. S. Kilic, B.D. Storey, and A. Ajdari. Towards an understanding of nonlinear electrokinetics at large voltages in concentrated solutions. *Advances in Colloid and Interface Science*, 152:48–88, 2009b.
- J. O.'M Bockris and A. K. N. Reddy. *Modern Electrochemistry*. Plenum, New York, 1970.
- A. B. D. Brown, C. G. Smith, and A. R. Rennie. Pumping of water with ac electric fields applied to asymmetric pairs of microelectrodes. *Phys. Rev. E*, 63:016305, 2000.
- D. N. Burch and M. Z. Bazant. Design principle for improved three-dimensional ac electro-osmotic pumps. *Phys. Rev. E*, 77:055303(R), 2008.
- B. P. Cahill, L. J. Heyderman, J. Gobrecht, and A. Stemmer. Electro-osmotic streaming on application of traveling-wave electric fields. *Physical Review E*, 70:036305, 2004.
- C. Q. Choi. Big lab on a tiny chip. *Scientific American*, October:100–103, 2007.
- K. T. Chu and M. Z. Bazant. Surface conservation laws at microscopically diffuse interfaces. *J. Colloid Interface Science*, 315:319–329, 2007.
- A.V. Delgado, F. González-Caballero, R.J. Hunter, L.K. Koopal, and J. Lyklema. Measurement and interpretation of electrokinetic phenomena. *J. Colloid Interface Sci.*, 309:194–224, 2007.
- A. S. Dukhin. Biospecific mechanism of double layer formation and peculiarities of cell electrophoresis. *Colloids and Surfaces A*, 73:29–48, 1993.

- A. S. Dukhin and S. S. Dukhin. Aperiodic capillary electrophoresis method using alternating current electric field for separation of macromolecules. *Electrophoresis*, 26:2149–2153, 2005.
- S. S. Dukhin and B. V. Derjaguin. *Surface and Colloid Science*, volume Vol. 7, chapter Ch. 2. Academic Press, New York, 1974.
- S. S. Dukhin and V. N. Shilov. Kinetic aspects of electrochemistry of disperse systems. part II. induced dipole moment and the non-equilibrium double layer of a colloid particle. *Adv. Colloid Interface Sci.*, 13:153–195, 1980.
- M. C. Fair and J. L. Anderson. Electrophoresis of heterogeneous colloids – doublets of dissimilar particles. *Langmuir*, 8:2850–2854, 1992.
- N. I. Gamayunov, V. A. Murtsovkin, and A. S. Dukhin. Pair interaction of particles in electric field. 1. features of hydrodynamic interaction of polarized particles. *Colloid J. USSR*, 48:197–203, 1986.
- N. I. Gamayunov, G. I. Mantrov, and V. A. Murtsovkin. Study of flows induced in the vicinity of conducting particles by an external electric field. *Colloid J.*, 54:20–23, 1992.
- S. Gangwal, O. J. Cayre, M. Z. Bazant, and O. D. Velev. Induced-charge electrophoresis of metallo-dielectric particles. *Phys. Rev. Lett.*, 100:058302, 2008.
- A. González, A. Ramos, N. G. Green, A. Castellanos, and H. Morgan. Fluid flow induced by non-uniform ac electric fields in electrolytes on microelectrodes. II. a linear double-layer analysis. *Phys. Rev. E*, 61:4019, 2000.
- D. C. Grahame. The electrical double layer and the theory of electrocapilarity. *Chem. Rev.*, 41:441–501, 1947.
- N. G. Green, A. Ramos, A. González, H. Morgan, and A. Castellanos. Fluid flow induced by nonuniform ac electric fields in electrolytes on microelectrodes. I. experimental measurements. *Phys. Rev. E*, 61:4011–4018, 2000a.
- N. G. Green, A. Ramos, and H. Morgan. AC electrokinetics: a survey of submicrometre particle dynamics. *J. Appl. Phys. D*, 33:632–641, 2000b.
- N. G. Green, A. Ramos, A. González, A. Castellanos, and H. Morgan. Fluid flow induced by nonuniform ac electric fields in electrolytes on microelectrodes. III. observation of streamlines and numerical simulation. *Phys. Rev. E*, 66:026305, 2002.
- M. M. Gregersen, F. Okkels, M. Z. Bazant, and H. Bruus. Topology and shape optimization of induced-charge electro-osmotic micropumps. *New Journal of Physics*, 11:075016, 2009.
- C. K. Harnett, J. Templeton, K. A. Dunphy-Guzman, Y. M. Senousya, and M. P. Kanouff. Model based design of a microfluidic mixer driven by induced charge electroosmosis. *Lab on a Chip*, 8:565–572, 2008.

- H. Helmholtz. Studien über elektrische grenzschichten. *Ann. Phys. Chem.*, 7 (ser. 3):337–382, 1879.
- C. C. Huang, M. Z. Bazant, and T. Thorsen. Ultrafast high-pressure ac electro-osmotic pumps for portable biomedical microfluidics. *Lab on a Chip*, 10:80–85, 2010.
- R. J. Hunter. *Foundations of Colloid Science*. Oxford University Press, Oxford, 2001.
- A. S. Khair and T. M. Squires. Fundamental aspects of concentration polarization arising from nonuniform electrokinetic transport. *Phys. Fluids*, 20:087102, 2008.
- M. S. Kilic and M. Z. Bazant. Induced-charge electrophoresis near an insulating wall. *arXiv:0712.0453v1*, [cond-mat.mtrl-sci], 2007.
- M. S. Kilic, M. Z. Bazant, and A. Ajdari. Steric effects in the dynamics of electrolytes at large applied voltages: I double-layer charging. *Phys. Rev. E*, 75:033702, 2007.
- B. J. Kirby and Ernest H. Hasselbrink. Zeta potential of microfluidic substrates: 1. theory, experimental techniques, and effects on separations. *Electrophoresis*, 25:187–202, 2004.
- D. J. Laser and J. G. Santiago. A review of micropumps. *J. Micromech Microeng*, 14:R35–64, 2004.
- V. G. Levich. *Physico-chemical Hydrodynamics*. Prentice-Hall, London, 1962.
- J. A. Levitan. *Experimental study of induced-charge electro-osmosis*. PhD thesis, MIT, 2005.
- J. A. Levitan, S. Devasenathipathy, V. Studer, Y. Ben, T. Thorsen, T. M. Squires, and M. Z. Bazant. Experimental observation of induced-charge electro-osmosis around a metal wire in a microchannel. *Colloids and Surfaces A*, 267:122–132, 2005.
- D. Long and A. Ajdari. Electrophoretic mobility of composite objects in free solution: Application to dna separation. *Electrophoresis*, 17:1161–1166, 1996.
- D. Long and A. Ajdari. Symmetry properties of the electrophoretic motion of patterned colloidal particles. *Phys. Rev. Lett.*, 81:1529–1532, 1998.
- J. Lyklema. *Fundamentals of Interface and Colloid Science. Volume II: Solid-Liquid Interfaces*. Academic Press Limited, San Diego, CA, 1995.
- J. R. Melcher and G. I. Taylor. Electrohydrodynamics: a review of the role of interfacial shear stresses. *Annu. Rev. Fluid Mech.*, 1:11146, 1969.
- F. A. Morrison and J. J. Stukel. Electrophoresis of an insulating sphere normal to a conducting plane. *J. Colloid and Interface Science*, 33:88, 1970.
- V. A. Murtsovkin. Nonlinear flows near polarized disperse particles. *Colloid Journal*, 58:341–349, 1996.

- V. A. Murtsovkin and G. I. Mantrov. Steady flows in the neighborhood of a drop of mercury with the application of a variable external electric field. *Colloid J. USSR*, 53:240–244, 1991.
- F. Nadal, F. Argoul, P. Hanusse, B. Pouligny, and A. Ajdari. Electrically induced interactions between colloidal particles in the vicinity of a conducting plane. *Phys. Rev. E*, 65, 2002.
- L. H. Olesen, H. Bruus, and A. Ajdari. AC electrokinetic micropumps: the effect of geometrical confinement faradaic current injection and nonlinear surface capacitance. *Phys. Rev. E*, 73:056313, 2006.
- A. J. Pascall and T. M. Squires. Induced charge electroosmosis over controllably-contaminated electrodes. *Phys. Rev. Lett*, 104:088301, 2010.
- H. A. Pohl. *Dielectrophoresis: the behaviour of neutral matter in nonuniform electric fields*. Cambridge University Press, 1978.
- A. Ramos, H. Morgan, N. G. Green, and A. Castellanos. AC electrokinetics: a review of forces in microelectrode structures. *J. Phys. D*, 31:2338–2353, 1998.
- A. Ramos, H. Morgan, N. G. Green, and A. Castellanos. AC electric-field-induced fluid flow in microelectrodes. *J. Colloid Interface Sci.*, 217:420–422, 1999.
- A. Ramos, H. Morgan, N. G. Green, A. Gonzalez, and A. Castellanos. Pumping of liquids with traveling-wave electro-osmosis. *Journal of Applied Physics*, 97:084906, 2005.
- W. D. Ristenpart, I. A. Aksay, and D. A. Saville. Electrically guided assembly of planar superlattices in binary colloidal suspensions. *Phys. Rev. Lett.*, 90:128303, 2003.
- K. A. Rose and J. G. Santiago. Rotational electrophoresis of striped metallic microrods. *Physical Review E*, 75:197–203, 2006.
- I. Rubinstein and B. Zaltzman. Electro-osmotic slip of the second kind and instability in concentration polarization at electro dialysis membranes. *Math. Mod. Meth. Appl. Sci.*, 11:263–300, 2001.
- D. Saintillan, E. Darve, and E. S. G. Shaqfeh. Hydrodynamic interactions in the induced-charge electrophoresis of colloidal rod dispersions. *Journal of Fluid Mechanics*, 563:223–259, 2006a.
- D. Saintillan, E. S. G. Shaqfeh, and E. Darve. Stabilization of a suspension of sedimenting rods by induced-charge electrophoresis. *Physics of Fluids*, 18:121701, 2006b.
- D. A. Saville. Electrohydrodynamics: The Taylor-Melcher leaky dielectric model. *Annu. Rev. Fluid Mech.*, 29:27–64, 1997.
- R. B. M. Schasfoort, S. Schlautmann, J. Hendrikse, and A. van den Berg. Field-effect flow control for microfabricated fluidic networks. *Science*, 286:942, 1999.

- R. B. Schoch, J. Y. Han, and P. Renaud. Transport phenomena in nanofluidics. *Rev. Mod. Phys.*, 80(3):839–883, 2008.
- V. N. Shilov and T. S. Simonova. Polarization of electric double layer of disperse particles and dipolophoresis in a steady (dc) field. *Colloid J. USSR*, 43:90–96, 1981.
- I. N. Simonov and V. N. Shilov. Theory of low-frequency dielectric-dispersion of a suspension of ideally polarizable spherical particles. *Colloid J. USSR*, 39:775–780, 1977.
- T. A. Simonova, V. N. Shilov, and O. A. Shramko. Low-frequency dielectrophoresis and the polarization interaction of uncharged spherical particles with an induced deby atmosphere of arbitrary thickness. *Colloid J.*, 63:108–115, 2001.
- M Smoluchowski. Zur theorie der elektrischen kataphorese und der oberflächenleitung. *Phys. Z.*, 6:529, 1905.
- T. M. Squires. Electrokinetics over inhomogeneously slipping surfaces. *Phys. Fluids*, 20:092105, 2008.
- T. M. Squires. Induced-charge electrokinetics: fundamental challenges and opportunities. *Lab on a Chip*, 9:2477, 2009. doi: DOI: 10.1039/b906909g.
- T. M. Squires and M. Z. Bazant. Induced-charge electro-osmosis. *J. Fluid Mech.*, 509:217–252, 2004.
- T. M. Squires and M. Z. Bazant. Breaking symmetries in induced-charge electro-osmosis and electrophoresis. *J. Fluid Mech.*, 560:65–101, 2006.
- T. M. Squires and S. R. Quake. Microfluidics: fluid physics on the nanoliter scale. *Rev. Mod. Phys.*, 77:977–1026, 2005.
- O. Stern. Zur theorie der elektrolytischen doppelschicht. *Z. Elektrochem.*, 30:508–516, 1924.
- H. A. Stone and A. D. T. Samuel. Propulsion of microorganisms by surface distortions. *Phys. Rev. Lett.*, 77:41024104, 1996.
- H.A. Stone, A.D. Stroock, and A. Ajdari. Engineering flows in small devices: Microfluidics toward a lab-on-a-chip. *Annu. Rev. Fluid Mech.*, 36:381411, 2004.
- B. D. Storey, Lee R. Edwards, M. S. Kilic, and M. Z. Bazant. Steric effects on ac electro-osmosis in dilute electrolytes. *Phys. Rev. E*, 77:036317, 2008.
- V. Studer, A. Pépin, Y. Chen, and A. Ajdari. An integrated ac electrokinetic pump in a microfluidic loop for fast tunable flow control. *Analyst*, 129: 944–949, 2004.
- Y. K. Suh and S. Kang. Asymptotic analysis of ion transport in a nonlinear regime around polarized electrodes under ac. *Phys. Rev. E*, 77:011502, 2008.
- Y. K. Suh and S. Kang. Numerical prediction of ac electro-osmotic flows around polarized electrodes. *Phys. Rev. E*, 79:046309, 2009.

- V. Tandon and B. J. Kirby. Zeta potential and electroosmotic mobility in microfluidic devices fabricated from hydrophobic polymers: 2. slip and interfacial water structure. *Electrophoresis*, 29:1102–1114, 2008.
- G. I. Taylor. Studies in electrohydrodynamics i. the circulation produced in a drop by an electric field. *Proc. Roy. Soc. A*, 291:15966, 1966.
- S. K. Thamida and H.-C. Chang. Nonlinear electrokinetic ejection and entrainment due to polarization at nearly insulated wedges. *Phys. Fluids*, 14:4315, 2002.
- M. Trau, D. A. Saville, and I. A. Aksay. Assembly of colloidal crystals at electrode interfaces. *Langmuir*, 13:6375, 1997.
- J. P. Urbanski, J. A. Levitan, M. Z. Bazant, and Todd Thorsen. Fast AC electro-osmotic pumps with non-planar electrodes. *Applied Physics Letters*, 89:143508, 2006a.
- J. P. Urbanski, J. A. Levitan, D. N. Burch, Todd Thorsen, and M. Z. Bazant. The effect of step height on the performance of AC electro-osmotic microfluidic pumps. *Journal of Colloid and Interface Science*, 309:332–341, 2006b.
- E. J. van der Wouden, D. C. Hermes, J. G. E. Gardeniers, and A. van den Berg. Directional flow induced by synchronized longitudinal and zeta-potential controlling ac-electrical fields. *Lab on a Chip*, 6:1300 – 1305, 2006.
- E.J. van der Wouden, T. Heuser, R.E. Oosterbroek D.C. Hermes, J.G.E. Gardeniers, and A. van den Berg. Field-effect control of electro-osmotic flow in microfluidic networks. *Colloids and Surfaces A: Physicochemical and Engineering Aspects*, 267:110–116, 2005.
- R. E. G. van Hal, J. C. T. Eijkel, and P. Bergveld. A general model to describe the electrostatic potential at electrolyte oxide interfaces. *Adv. Colloid Interface Sci.*, 69:31–62, 1996.
- P. K. Wong, T. H. Wang, J. H. Deval, and C. M. Ho. Electrokinetics in microdevices for biotechnology applications. *IEEE/AMSE Transactions on Mechatronics*, 9:366–376, 2004.
- J. Wu. Biased AC electro-osmosis for on-chip bioparticle processing. *IEEE Transactions on Nanotechnology*, 5:84–88, 2006.
- Z. Wu and D. Li. Micromixing using induced-charge electrokinetic flow. *Electrochimica Acta*, 53(19):5827–5835, AUG 1 2008a.
- Z. Wu and D. Li. Mixing and flow regulating by induced-charge electrokinetic flow in a microchannel with a pair of conducting triangle hurdles. *Microfluidics and Nanofluidics*, 5(1):65–76, JUL 2008b.
- S. H. Yao and J. G. Santiago. Porous glass electroosmotic pumps: theory. *Journal of Colloid and Interface Science*, 268(1):133–142, DEC 1 2003. ISSN 0021-9797.

- E. Yariv. Induced-charge electrophoresis of nonspherical particles. *Phys. Fluids*, 17:051702, 2005.
- E. Yariv. Nonlinear electrophoresis of ideally polarizable particles. *Europhysics Letters*, 82(5):54004, JUN 2008. ISSN 0295-5075.
- S. Yeh, M. Seul, and B. Shraiman. Assembly of ordered colloidal aggregates by electric-field-induced fluid flow. *Nature (London)*, 386:57, 1997.
- G. Yossifon, I. Frankel, and T. Miloh. On electro-osmotic flows through microchannel junctions. *Phys. Fluids*, 18:117108, 2006.
- B. Zaltzman and I. Rubinstein. Electro-osmotic slip and electroconvective instability. *Journal of Fluid Mechanics*, 579:173–226, 2007.
- H. Zhao and H. H. Bau. On the effect of induced electro-osmosis on a cylindrical particle next to a surface. *Langmuir*, 23:4053–4063, 2007a.
- H. Zhao and H. H. Bau. Microfluidic chaotic stirrer utilizing induced-charge electro-osmosis. *Phys. Rev. E*, 75:066217, 2007b.